

DEVELOPMENT OF A SIMPLIFIED PLASMA OPENING
SWITCH USING AN INVERSE PINCH AS A PLASMA
SOURCE

Approved for public release; distribution is unlimited.

September 2000



Prepared for:
Defense Threat Reduction Agency
45045 Aviation Drive
Dulles, VA 20166-7517

DNA 001-95-C-0014

John J. Moschella, et. al.

Prepared by: HY-Tech Research Corporation
104 Centre Court
Radford, VA 24141

20010308 042

DESTRUCTION NOTICE:

Destroy this report when it is no longer needed. Do not return to sender.

PLEASE NOTIFY THE DEFENSE THREAT REDUCTION AGENCY, ATTN: ADM, 45045 AVIATION DRIVE, DULLES, VA 20166-7517, IF YOUR ADDRESS IS INCORRECT, IF YOU WISH IT DELETED FROM THE DISTRIBUTION LIST, OR IF THE ADDRESSEE IS NO LONGER EMPLOYED BY YOUR ORGANIZATION.

DISTRIBUTION LIST UPDATE

This mailer is provided to enable DTRA to maintain current distribution lists for reports. (We would appreciate you providing the requested information.)

- ☐ Add the individual listed to your distribution list.
- ☐ Delete the cited organization/individual.
- ☐ Change of address.

Note:

Please return the mailing label from the document so that any additions, changes, corrections or deletions can be made easily. For distribution cancellation or more information call DTRA/ADM (703) 325-1036.

NAME: _____

ORGANIZATION: _____

OLD ADDRESS

NEW ADDRESS

TELEPHONE NUMBER: () _____

DTRA PUBLICATION NUMBER/TITLE

CHANGES/DELETIONS/ADDITIONS, etc.)

(Attach Sheet if more Space is Required)

DTRA or other GOVERNMENT CONTRACT NUMBER: _____

CERTIFICATION of NEED-TO-KNOW BY GOVERNMENT SPONSOR (if other than DTRA):

SPONSORING ORGANIZATION: _____

CONTRACTING OFFICER or REPRESENTATIVE: _____

SIGNATURE: _____

CUT HERE AND RETURN

DEFENSE THREAT REDUCTION AGENCY
ATTN: ADM
45045 AVIATION DRIVE
DULLES, VA 20156-7517

DEFENSE THREAT REDUCTION AGENCY
ATTN: ADM
6801 TELEGRAPH ROAD
ALEXANDRIA, VA 22310-3398

REPORT DOCUMENTATION PAGE			Form Approved OMB No 0704-0188	
Public reporting burden for this collection of information is estimated to average 1 hour per response, including the time for reviewing instructions, searching existing data sources, gathering and maintaining the data needed, and completing and reviewing the collection of information. Send comments regarding this burden estimate or any other aspect of this collection of information, including suggestions for reducing this burden, to Washington Headquarters Services, Directorate for Information Operations and Reports, 1215 Jefferson Davis Highway, Suite 1204, Arlington, VA 22202-4302, and to the Office of Management and Budget, Paperwork Reduction Project (0704-0188), Washington, DC 20503.				
1 AGENCY USE ONLY (Leave blank)		2 REPORT DATE 980807		3 REPORT TYPE AND DATES COVERED Technical 950221 - 980730
4 TITLE AND SUBTITLE Development of a Simplified Plasma Opening Switch Using an Inverse Pinch as a Plasma Source			5 FUNDING NUMBERS C - DNA 001-95-C-0014 PE - 4662 PR - AB TA - IE WU - DH60854	
6 AUTHOR(S) John J. Moschella, Edward J. Yadlowsky, and Robert C. Hazelton				
7 PERFORMING ORGANIZATION NAME(S) AND ADDRESS(ES) HY-Tech Research Corporation 104 Centre Court Radford, VA 24141			8 PERFORMING ORGANIZATION REPORT NUMBER	
9 SPONSORING/MONITORING AGENCY NAME(S) AND ADDRESS(ES) Defense Threat Reduction Agency 45045 Aviation Drive Dulles, VA 20166-7517 NSSS/Schneider			10 SPONSORING/MONITORING AGENCY REPORT NUMBER DSWA-TR-98-71	
11 SUPPLEMENTARY NOTES This work is sponsored by the Defense Threat Reduction Agency under RDT&E RMC code B 4622 D AB IE 8010 A AF 25904D.				
12a DISTRIBUTION/AVAILABILITY STATEMENT Approved for public release; distribution is unlimited.			12b DISTRIBUTION CODE	
13 ABSTRACT (Maximum 200 words) The design, development, and testing of the "inverse pinch" plasma source for plasma opening switches is described. This source relies on the breakdown of a gas to form a plasma in an arrangement that is the inverse of a gas puff z-pinch. The plasma produced by the IP is best described as an expanding plasma ring and it has been designed to work with switches that have an <i>IT</i> product greater than 1 MA-μs. As a result, when using this source with a cylindrical POS, a single device mounted inside the center conductor is required as the ejected plasma matches the symmetry of the transmission line. The plasma produced by the IP was characterized on a test bed using framing photography, magnetic pick-up loops, spectroscopy, as well as single and dual beam heterodyne interferometry in various configurations. The results from field testing on the Hawk cylindrical POS with a shorted load is also reported. The POS experiments with a short circuit load indicated superior performance using a hydrogen plasma with strong dependence on the initial conditions. The data also implies that the conduction phase of the POS is influenced by secondary plasma formation from electrode surfaces. Further experimentation using the IP with H ₂ gas is planned.				
14 SUBJECT TERMS Inverse Pinch POS Plasma Source			15 NUMBER OF PAGES 74	
			16 PRICE CODE	
17 SECURITY CLASSIFICATION OF REPORT UNCLASSIFIED	18 SECURITY CLASSIFICATION OF THIS PAGE UNCLASSIFIED	19 SECURITY CLASSIFICATION OF ABSTRACT UNCLASSIFIED	20 LIMITATION OF ABSTRACT SAR	

Conversion Table

Conversion factors for U.S. Customary to metric (SI) units of measurement.

MULTIPLY TO GET \longleftrightarrow BY BY \longleftrightarrow TO GET DIVIDE

angstrom	1.000 000 X E -10	meters (m)
atmosphere (normal)	1.013 25 X E +2	kilo pascal (kPa)
bar	1.000 000 X E +2	kilo pascal (kPa)
barn	1.000 000 X E -28	meter ² (m ²)
British thermal unit (thermochemical)	1.054 350 X E +3	joule (J)
calorie (thermochemical)	4.184 000	joule (J)
cal (thermochemical/cm ²)	4.184 000 X E -2	mega joule/m ² (MJ/m ²)
curie	3.700 000 X E +1	*giga becquerel (GBq)
degree (angle)	1.745 329 X E -2	radian (rad)
degree Fahrenheit	$t_k = (t^o_f + 459.67)/1.8$	degree kelvin (K)
electron volt	1.602 19 X E -19	joule (J)
erg	1.000 000 X E -7	joule (J)
erg/second	1.000 000 X E -7	watt (W)
foot	3.048 000 X E -1	meter (m)
foot-pound-force	1.355 818	joule (J)
gallon (U.S. liquid)	3.785 412 X E -3	meter ³ (m ³)
inch	2.540 000 X E -2	meter (m)
jerk	1.000 000 X E +9	joule (J)
joule/kilogram (J/kg) radiation dose absorbed	1.000 000	Gray (Gy)
kilotons	4.183	terajoules
kip (1000 lbf)	4.448 222 X E +3	newton (N)
kip/inch ² (ksi)	6.894 757 X E +3	kilo pascal (kPa)
ktap	1.000 000 X E +2	newton-second/m ² (N-s/m ²)
micron	1.000 000 X E -6	meter (m)
mil	2.540 000 X E -5	meter (m)
mile (international)	1.609 344 X E +3	meter (m)
ounce	2.834 952 X E -2	kilogram (kg)
pound-force (lbs avoirdupois)	4.448 222	newton (N)
pound-force inch	1.129 848 X E -1	newton-meter (N·m)
pound-force/inch	1.751 268 X E +2	newton/meter (N/m)
pound-force/foot ²	4.788 026 X E -2	kilo pascal (kPa)
pound-force/inch ² (psi)	6.894 757	kilo pascal (kPa)
pound-mass (lbm avoirdupois)	4.535 924 X E -1	kilogram (kg)
pound-mass-foot ² (moment of inertia)	4.214 011 X E -2	kilogram-meter ² (kg·m ²)
pound-mass/foot ³	1.601 846 X E +1	kilogram/meter ³ (kg/m ³)
rad (radiation dose absorbed)	1.000 000 X E -2	**Gray (Gy)
roentgen	2.579 760 X E -4	coulomb/kilogram (C/kg)
shake	1.000 000 X E -8	second (s)
slug	1.459 390 X E +1	kilogram (kg)
torr (mm Hg, 0° C)	1.333 22 X E -1	kilo pascal (kPa)

*The becquerel (Bq) is the SI unit of radioactivity; 1 Bq = 1 event/s.

**The Gray (GY) is the SI unit of absorbed radiation.

Table of Contents

Section	Page
Conversion Table	ii
Figures	vi
Tables	vii
 1 Executive Summary	 1
 2 Introduction	 3
 3 Overview of Inverse Pinch Operation	 5
 4 Design of the Inverse Pinch	 9
4.1 The Gas Delivery System.	9
4.2 Electrode and Cable Feed Design.	11
4.3 Evolution of the Inverse Pinch.	11
 5 Diagnostics for the Inverse Pinch	 15
5.1 Rogowski Current Monitor.	15
5.2 Visible Light Framing Camera.	15
5.3 Magnetic Pick-Up Loops.	16
5.4 Time Resolved Heterodyne Interferometer.	18
5.5 Two Wavelength Interferometry.	22
5.6 Spectroscopic Measurements.	23
 6 Experimental Measurements	 24
6.1 Neutral Gas Measurements.	24
6.2 Measurements on the Expanding Plasma Shell.	25
6.2.1 Visible Light Framing Photography.	27
6.2.2 Magnetic Pick-up Loops.	27
6.2.3 Chordal Line-of-Sight Interferometry.	29
6.3 Measurements on the Exhaust Plasma.	29

Table of Contents (Continued)

Section	Page
6.3.1 Exhaust Measurements Using Heterodyne Interferometry.	31
6.3.2 Snowplow Model for the IP.	35
6.4 Measurements in a POS-like Configuration.	39
6.4.1 The Axial Distribution of Plasma in a POS Gap.	40
6.4.2 Plasma Radial Distribution.	45
6.4.3 Plasma Azimuthal Symmetry.	47
6.4.4 Spectroscopic Measurements on the H Plasma.	47
6.4.5 Plasma Reproducibility.	52
6.4.6 Mass Density Control.	52
7 Results of POS Experiments on Hawk	54
7.1 Hardware and Diagnostics.	54
7.2 POS Shots Using the IP.	55
7.2.1 Density Evolution: Conduction Phase for IP/H ₂ Shots.	59
7.2.2 Density Evolution: Opening Phase for IP/H ₂ Shots.	61
7.2.3 Density Evolution: IP/Ar Shots.	62
7.2.4 Scaling of POS Current.	63
7.2.5 Comments on IP/Air and IP/Ne Shots.	64
8 Conclusions	66
Appendix	
Bibliography	68
Distribution List	70

Figures

Figure		Page
1	Configuration of the IP inside Hawk	4
2	Scaled drawing of the inverse pinch	5
3	Operational mechanism of the IP	6
4	Current vs. time for an IP discharge	7
5	Detail of the General Valve series 9 gas valve	10
6	An early version of the inverse pinch with 20 cm diameter electrode plates .	12
7	Circuit schematic of puff valve pulser	13
8	Experimental set up of the high-speed framing camera	16
9	Configurations used for B-dot loops	17
10	Schematic of the He-Ne interferometer	19
11	Schematic of the two channel He-Ne interferometer	20
12	Various configurations used for interferometry	21
13	Schematic of the spectroscopic apparatus	22
14	Interferometer beam positions used for neutral gas measurements	25
15	H ₂ density vs. radius from neutral gas measurements	26
16	H ₂ mass/length vs. time from neutral gas measurements	27
17	Visible light frame photos of the expanding plasma shell	28
18	Results from the magnetic pick-up loop array on the expanding plasma . . .	30
19	Chordal line-of-sight interferometry signals on the expanding plasma	31
20	Abel inverted density profiles of the expanding plasma for various gases . . .	32
21	Plasma position and velocity as determined via chordal interferometry	33
22	Plasma density as a function of time for the IP discharge	34
23	Illustration of a 1D snowplow	35
24	Electrical circuit for the inverse pinch	36
25	Neutral gas distribution used for the snowplow calculation	37

Figures (Continued)

Figure	Page
26 Results of the 1D snowplow calculation	38
27 The IP mounted in a "mocked-up" POS	41
28 Laser beam positions used to measure the axial distribution	41
29 Plasma axial distribution with a 95% transparent inner boundary	42
30 Results from axially resolved B-dot loops	43
31 Model explaining axial spreading	44
32 The IP with a screened inner boundary	45
33 Relative axial distribution of plasma in a POS gap with a screened inner boundary (various gases)	46
34 Hydrogen plasma radial distribution in a POS gap at various times	48
35 Results from two channel interferometry with a 30° beam separation	48
36 Hydrogen plasma density in a POS gap vs. puff valve pressure	52
37 Load current traces obtained using the IP and cable guns on Hawk	58
38 Peak POS voltage vs. conduction time for IP/H ₂ shots on Hawk	58
39 Electron density vs. time from the 8-channel interferometer for an IP/H ₂ shot on Hawk	59
40 Electron density vs. radius at various times during an IP/H ₂ shot on Hawk .	60
41 Electron inventory vs. time during an IP/H ₂ shot on Hawk	62
42 Conducted current vs. initial electron density for IP data on Hawk with MHD theory	64

Tables

Table		Page
1	Data on exhaust plasma for various gases and predicted ionization level . . .	39
2	Identified impurity emission lines observed with the “dirty” IP	49
3	Data of obtainable mass densities in the mocked-up POS geometry	53
4	IP/Hawk shot data	56

Section 1

Executive Summary

The inverse pinch (IP) is a new type of plasma source that has been designed specifically for cylindrical plasma opening switches. While inverse pinch geometry has been used in the past for dense plasma focus studies [1] and low inductance closing switches,[2] to our knowledge this is the first device intended as a plasma source. During the course of this program, we designed, built, and tested the source at HY-Tech's laboratories and fielded it on the Hawk POS at the Naval Research Laboratory. The tests on Hawk, using the IP with H_2 gas, were very successful and have stimulated a great deal of interest and further experimentation.

When compared to plasma sources most often used for POS research, namely cable guns and flashboards, the IP is significantly different in a number of ways and represents an entirely different approach. The most obvious difference is that the IP is a monolithic source, with symmetry that matches the transmission line, and it must be mounted inside the center conductor. The more traditional scheme requires numerous sources that are arranged around the outer conductor. The IP mounting scheme reverses the directed velocity of the plasma, and shifts the dominant impurity source from the inner to the outer conductor. The IP is also a gas source, where the other sources are surface discharge sources. This is potential advantage because the plasma species can be varied by changing the type of gas, and evidence from past experiments suggested that lighter ions improved switch characteristics.[3] Another key difference, that may be the most important, is due to the nature of the IP plasma. We are referring here to the fact that the plasma ejected from the IP is best characterized as an expanding ring with very little plasma in its wake. When the IP was mounted in a Hawk-like POS configuration, we observed re-strike plasmas that were ejected about $3.5 \mu s$ after the first plasma ring. This additional plasma was inconsequential on Hawk, as the entire conduction and opening phase of the POS occurred before this plasma arrived, and if need be it can always be removed via a crow-barred circuit. The discrete ring nature of the plasma allowed us control the initial plasma distribution simply by varying the delay time between the source and the generator. It also enabled us, by going to long delays, to fill the POS gap uniformly with a plasma that was quasi-static on the time scales of the experiment

(1 μs). This is not possible with other POS sources. As it turned out, it was this uniform, quasi-static, initial plasma that produced the best results in an opening switch.

While the version of the inverse pinch that was used on Hawk showed great promise, it needs further investigation before it can be considered a replacement for cable guns or flashboards. Due to the rather significant engineering effort that must be undertaken to use the IP with a diode load, a short circuit load was used for the initial experiments on Hawk. A short circuit load develops a relatively small voltage at the switch, and more experiments are needed to fully investigate this source. As of this writing experiments are starting that will use the IP on Hawk with an electron beam diode load.

We would also like to add that, in its present configuration, the IP is hardly optimized. There are many improvements that can be made. One of these is a structure to prevent build up of neutral gas in the inter-electrode region of the IP, a so-called gas dump. A successful re-design of the electrode opposite the puff valve nozzle may lengthen the usable range of puff valve delays and reduce possible gas contamination in the POS gap. It may also result in more consistent breakdowns and plasma reproducibility by reducing high gas pressures on the quartz insulator. A re-design of the puff valve/nozzle system may also improve the source. This system was essentially designed without the aid of computer simulations and neutral gas measurements. In fact, the neutral gas measurements made at NRL suggest that the gas shell spreads radially causing significant gas densities on the quartz insulator, which is undesirable. Finally, a gas pre-ionization would probably result in vastly improved consistency with regards to plasma production from shot to shot. These improvements, while outside the scope of this initial program, should be seriously considered if the IP is successful in future experiments.

Section 2

Introduction

This report describes the design and operation of the inverse pinch (IP) plasma source and POS experiments conducted on the Hawk generator at NRL. This source was developed under DSWA contract #DNA001-95-C-0014 and was designed to replace arrays of flashboards and cables guns commonly used to fill POS gaps. The inverse pinch produces a radially expanding plasma ring that can be used to fill a POS gap if the IP is placed inside the center conductor of the pulsed power machine. Such a configuration is depicted in Figure 1 that shows the IP inside the Hawk center conductor. This report will describe the general operation of the IP with emphasis on the characteristics of the plasma that are most important to POS applications, and results of the first tests of the source on the Hawk generator. Therefore, we will report measurements on the plasma properties, and pertinent measurements on the distribution of neutral gas prior to the application of the high-voltage pulse. These plasma properties will include the mass density, axial distribution, radial distribution, azimuthal symmetry, and shot-to-shot reproducibility using the IP configured in a POS-like environment. We will also show POS characteristics from the Hawk experiments. The data summarized in this report was compiled over approximately a two and one half year period from 9/95 to 5/98.

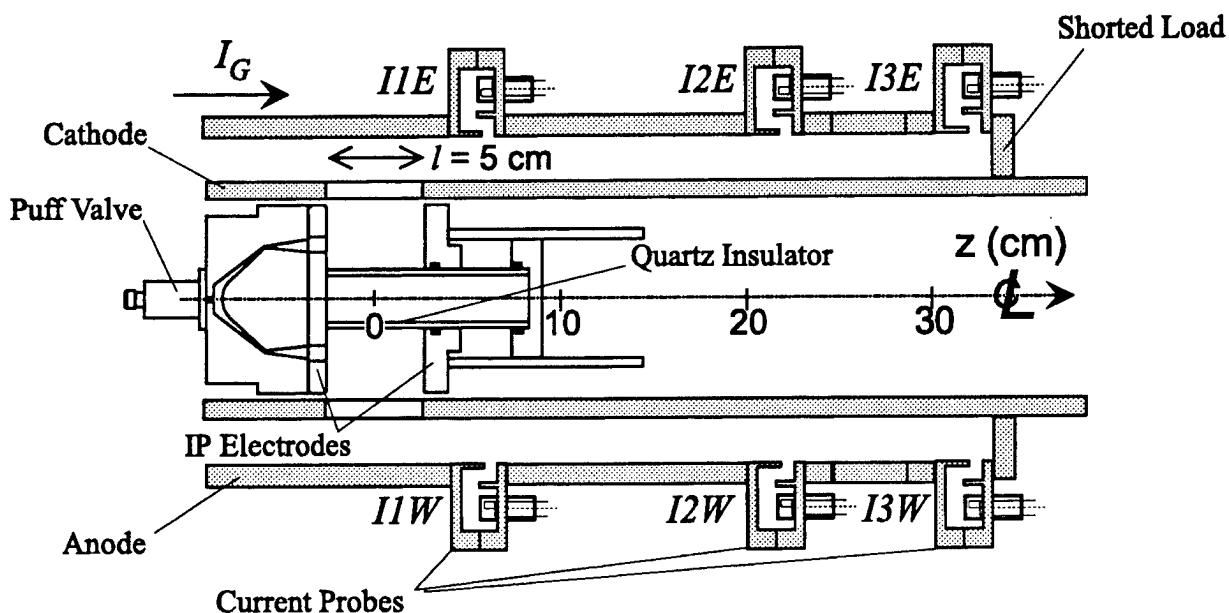


Figure 1. The configuration of the inverse pinch inside the cylindrical plasma opening switch on Hawk. The plasma is ejected radially outward through a semi-transparent inner conductor (cathode). The capacitor bank and spark gap switch were located outside the vacuum system and the load cables (12x RG-58) were fed through the vacuum inside the cathode.

Section 3

Overview of Inverse Pinch Operation

The version of the IP used to obtain most of the data presented in this report is shown in Figure 2. A version with slightly reduced electrode dimensions, shown in Figure 1, was installed on Hawk. The plasma was formed between two concentric brass disks supported by a 3.0 cm diameter quartz tube. Over the course of the program the diameter of the electrodes varied from 20 to 9.5 cm, but the diameter of the gas exhaust and quartz insulator was unchanged throughout. A high voltage pulse was applied across the two disks via the cable feed section that provided a connection for 12 RG-58 type cables. The cables were connected to a spark gap switch/capacitor bank assembly that consisted of a single $7.4 \mu\text{F}$ capacitor and spark gap switch. The bank was typically charged to 20 kV, and its discharge was initiated by a trigger pulse from a PT-55.

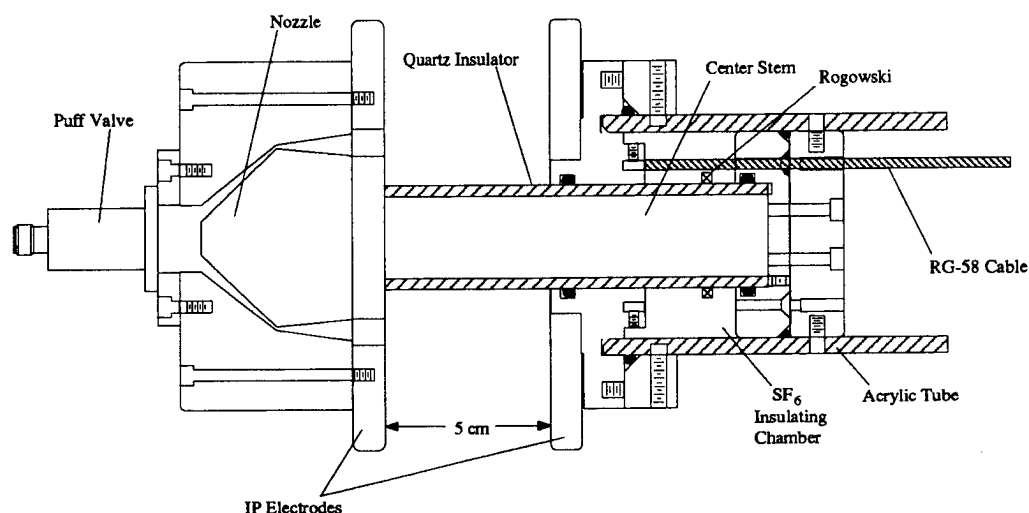
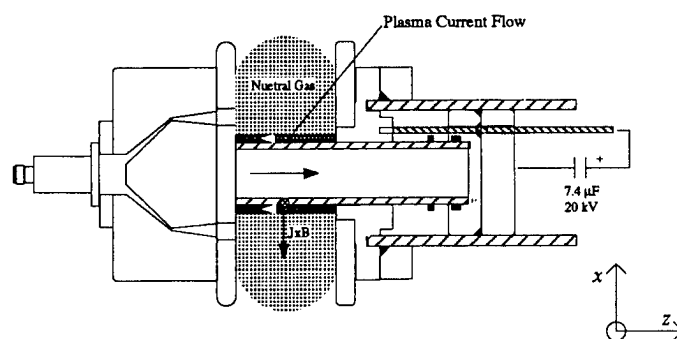
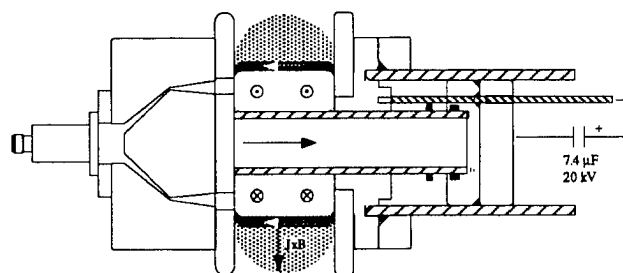


Figure 2. The version inverse pinch device, with 12.7 cm diameter electrodes, that was used for most of the tests at HY-Tech. The plasma is formed between the two, disc shaped, electrodes and expands radially outward. The SF_6 chamber prevents electrical breakdowns along the feed cables in the vacuum.

(a)



(b)



(c)

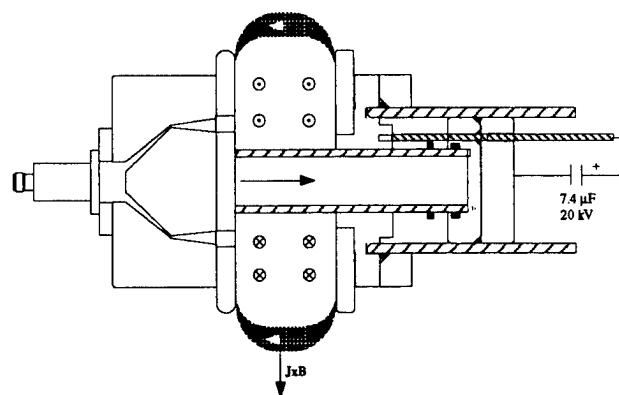


Figure 3. A series of illustrations outlining the basic operation of the IP. In (a), an electrical breakdown is initiated along the quartz insulator by discharging a 20 kV capacitor bank after the release of a gas puff. In (b), the current shell is forced radially out by magnetic pressure as it ionizes the neutral gas in its path. In (c), the plasma ring is ejected when the current shell reaches the edge of the electrode plates.

Approximately 350-700 μs before the high-voltage spark gap switch was closed, a fast acting puff valve discharged a volume of gas between the two disks. This delay time was needed to allow enough gas to enter the inter-electrode region, and its magnitude depended on the type of gas and pressure behind the valve. A nozzle directed the annular gas puff so it entered the intra-disk region approximately 1 cm from the surface of the quartz tube via a series of 18 holes in the electrode plate. This hole pattern consisted of 5/16" diameter holes with a bolt circle diameter of 4.6 cm. When the high voltage was applied, an electrical breakdown in the gas occurred on the quartz tube creating a plasma in the form of a conducting cylinder. This process was verified by optical framing photography. Since the current flowing through the cylinder is returned along a brass center stem inside the quartz insulator, the plasma is forced radially outward by magnetic pressure. This situation is the exact inverse of a typical gas puff z-pinch. As the conducting cylinder expands, it ionized the gas forming an expanding plasma ring as depicted in Figure 3. Typically, this process took 1-2 μs for the plasma to be ejected from the IP depending on the type of gas. Heavier gases tended to take longer to expand due to a larger mass that the puff valve/nozzle system could supply.

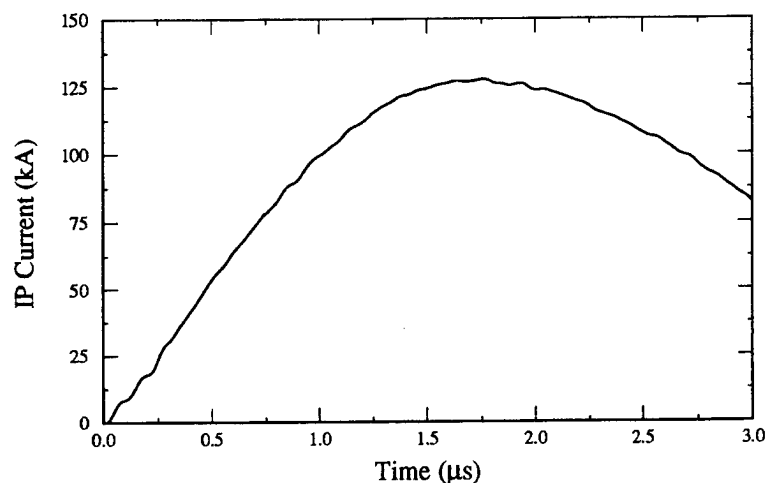


Figure 4. A plot of the current vs. time recorded during an IP discharge. When using H_2 gas, plasma is typically ejected $\sim 1 \mu\text{s}$ after the start of current.

The total current flowing through the IP was monitored using an integrated Rogowski coil positioned inside the cable feed section as shown in Figure 2. Figure 4 shows a typical current trace that we obtained during a 20 kV discharge. The current peaks at approximately 125 kA in 1.7 μs .

One important aspect of the operation of the IP was that the plasma was emitted as a discrete ring. This proved to be a very important property because in a POS configuration, the delay time between the initiation of the plasma source and the generator could be used to control the initial distribution of plasma, independent of the quantity of plasma. Depending on the geometrical arrangement of the source, additional breakdowns and plasma formation during the second half cycle have been observed, particularly in the Hawk geometry. However, with no confining boundary we never observed "re-strike" plasma. The characteristics of the expanding plasma ring are somewhat dependent on the type of gas. In general the ring is 2 cm long immediately after exit and expands radially at a rate of 1-7 cm/ μ s. These results were obtained from interferometric measurements that will be described in later sections.

An important aspect of the IP in POS geometry is the configuration of center conductor windows that allow the plasma to enter the POS gap. These need to be designed so the IP current front is terminated at the windows and does not bow into the POS gap. We found that bowing of the front into the gap lead to unacceptable axial acceleration of the plasma. For instance, the center conductor on Hawk was designed with 18 openings supported by 3 mm bars. When the IP current front reaches the windows, the current continues to flow in the bars while the plasma passes into the inter-electrode region. We tested a similar design with 8 windows and found the the plasma was axially accelerated. In that case the larger spacing between the windows allowed the IP current to bow into the POS gap and push the plasma axially.

Section 4

Design of the Inverse Pinch

This section will describe the design of the inverse pinch including a review of the evolution of the source up to the final design that was installed on Hawk.

4.1 The Gas Delivery System.

The main function of the pulsed gas valve and nozzle is to introduce a volume of gas between the disc shaped electrodes. The system designed for the IP, shown in Figure 2, was able to accomplish this task while meeting these other constraints:

1. The valve/nozzle system introduced a large enough mass to reach plasma densities of interest.
2. The valve delays could be adjusted, and the rise time of the gas was fast enough, to maintain vacuum pressure in the remainder of the system with minimal contamination.
3. The valve/nozzle system operated reliably in a pulsed power environment.

Many valve systems have been designed for Z-pinch applications that produce annular gas puffs as we required for the IP. However, the requirements for these systems are much more stringent with respect to the spatial distribution of gas, and they typically emit quantities of gas far in excess of that required for the IP. For the IP we only need a few hundred mT of gas on average between the electrode plates to produce acceptable quantities of plasma. We designed the IP valve/nozzle system around the commercially available General Valve series 9 pulsed gas valve shown in Figure 5.[4] Physically the valve is small, it is slightly less than 5 cm long and mounts to a flange with a 2.5 cm diameter bolt circle. The valve has an effective plenum volume of 0.35 cm^{-3} and an orifice diameter of 0.8 mm. The valve shell is threaded and is easily unscrewed from the valve body. A series of shims can be used to adjust the position of the shell with respect to the body, and this allows one to calibrate the gas output of the valve. It allowed us to optimize the valve operation for high pressure operation. According to the manufacturer, when the valve is supplied with a 300 volt, 160 μs duration electrical pulse, the orifice was fully opened in 160 μs . During this time the

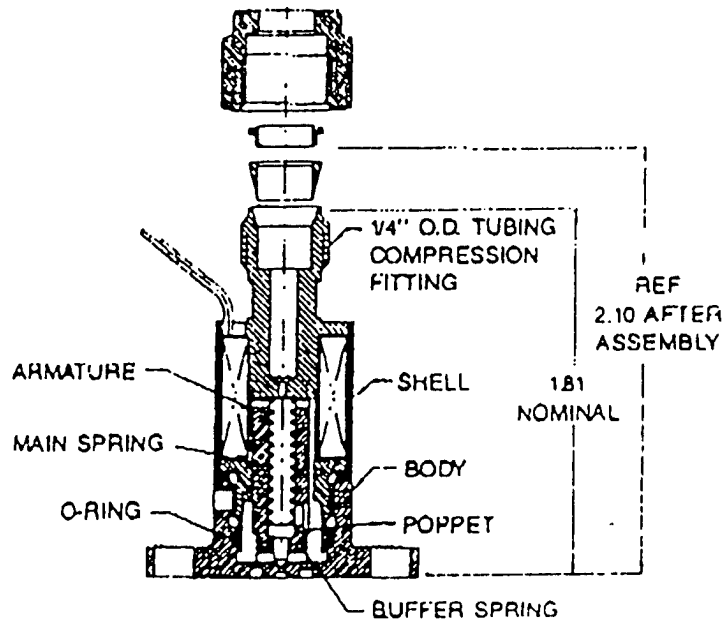


Figure 5. The series 9 puff valve manufactured by General Valve Inc., NJ.

poppet moves a total of 0.13 mm. Various poppet materials were available, we found that a PEEK poppet worked best for high pressure applications since it deformed less than the Teflon poppet. This valve is also inexpensive, reliable (lifetimes in excess of 10^5 shots), and the usable range of gas pressures is 50-1000 psig. This enabled us to operate the Hawk POS with H_2 and Ar gas simply by adjusting pressures using 800 and 50 psig for the two respectively. For the driver we used a 300 volt pulse from a $3.3 \mu F$ capacitor with a 2Ω resistor in series to limit the current in the 180 mH valve coil.

The nozzle was designed with primary emphasis on providing a duct for the gas to the inter-electrode region of the IP. This was accomplished while maintaining a gradient in the gas density so a Paschen minimum close to the quartz insulator resulted. Thus, the exit holes for the gas were centered 1 cm away from the quartz so the gas density decreased radially inward from the gas exit holes. This was important because the IP was designed without gas pre-ionization and must therefore rely on a Paschen breakdown. If the gas pressure on the quartz insulator becomes too large, then it is likely that electrical discharge would initiate at a larger radius where the gas density is decreasing. This would result in an expanding current shell with most of the neutral gas inside the shell, and no chance of it being incorporated into the snow plowed plasma. In fact, we have observed that as the puff valve delay is lengthened, and the amount of gas in the inter-electrode region increased, the plasma production reaches a point where it begins to decrease. This was most likely due

to high gas pressures on the quartz insulator at the time the voltage is switched on. This phenomenon places a practical restriction on the effective range of puff valve delays for a given gas. However, it should be noted that the requirement of minimal gas contamination in the POS region was more restrictive in the Hawk geometry. Measurements of the neutral gas distribution using an ultra-sensitive interferometer at NRL, show that the gas exiting the nozzle spreads out radially very quickly over the 5 cm gap between the electrode plates. This indicated that a re-designed nozzle, one that would collimate the gas more effectively to reduce build-up on the quartz insulator, would probably improve the overall operation of the IP.

4.2 Electrode and Cable Feed Design.

The inverse pinch electrodes were constructed from brass discs. Brass was chosen because it is a good electrical conductor and is more resistant to ablation and thermal desorption than aluminum. The puff valve/nozzle system was mounted to one of these discs that had series of holes to allow the gas to enter the device (IP anode), while the other had a hole cut in the center (IP cathode). The quartz insulator and brass center stem were fed through this hole. Since the center stem was electrically connected to the anode plate, the electrical connections were made from one side of the device.

The cable feed section is shown in Figure 2. In this section the center conductors of 12 RG-58 type cables were fed through the end flange and electrically connected to the cathode plate. A small solid brass cylinder was soldered to the end of each center conductor so it could be fastened to the IP anode using set screws. The braids for these cables were connected to the anode plate via the end flange and center stem. For this connection we soldered a slotted brass tube to each braid which was press fit into holes in the end flange. This allowed us to easily plug and un-plug these connections. The area surrounding the cathode connections was enclosed with an acrylic tube which was sealed to the end flange and cathode plate with o-rings. Additional o-rings were placed around the polyethylene on each of the RG-58 cables and the quartz insulator to form a small, sealed chamber that was pressurized with 40 psig of SF_6 . We found that the SF_6 chamber allowed us to operate the IP up to 25 kV without breakdowns.

4.3 Evolution of the Inverse Pinch.

The final design of the inverse pinch evolved over the course of the program. Most of the data contained in this report will reflect measurements conducted on the version shown in

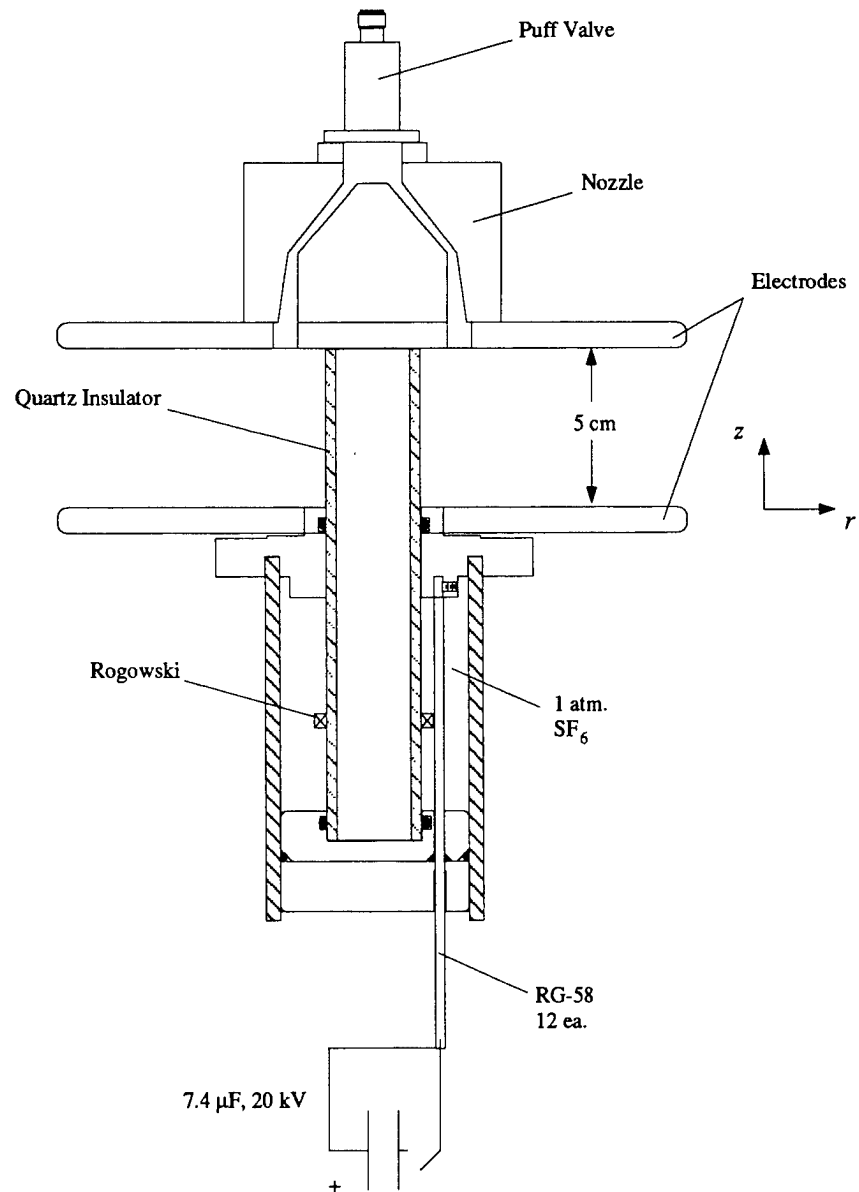


Figure 6. A scaled drawing of an early IP design that used 20.3 cm diameter electrode plates. The cable feed section is also longer than in later versions.

Figure 2. In this section we will briefly summarize the changes made during course of the program that improved the source. The first incarnation of the IP had 20.3 cm diameter electrode plates, did not have the sealed SF₆ chamber, and the nozzle had a slightly larger throat dimension than later versions. We quickly discovered that electrical breakdowns were occurring along the feed cable section which was at that time in vacuum. The sealed SF₆ chamber was immediately added and the version shown in Figure 6 resulted. This not only eliminated the breakdown problem, but for later versions it allowed us to shorten the feed section and lower the inductance. Subsequent measurements on the plasma density between the electrode plates showed that, in a typical operating regime, the snowplow front continued to accumulate plasma up to a radius of about 4-5 cm. As a result we decide to reduce the diameter of the electrode plates to 5" (6.3 cm radius). This change essentially had no impact on the operation, but made the device smaller and more practical. During the same time period, simulations of the gas flow by Hylton Murphy at Maxwell Technologies (using 2DRZ) on the nozzle showed an unstable behavior that was removed in the simulations by using a narrower throat. We therefore reduced that nozzle throat size from 0.050" to 0.034" which resulted in a noticeable more consistent behavior.

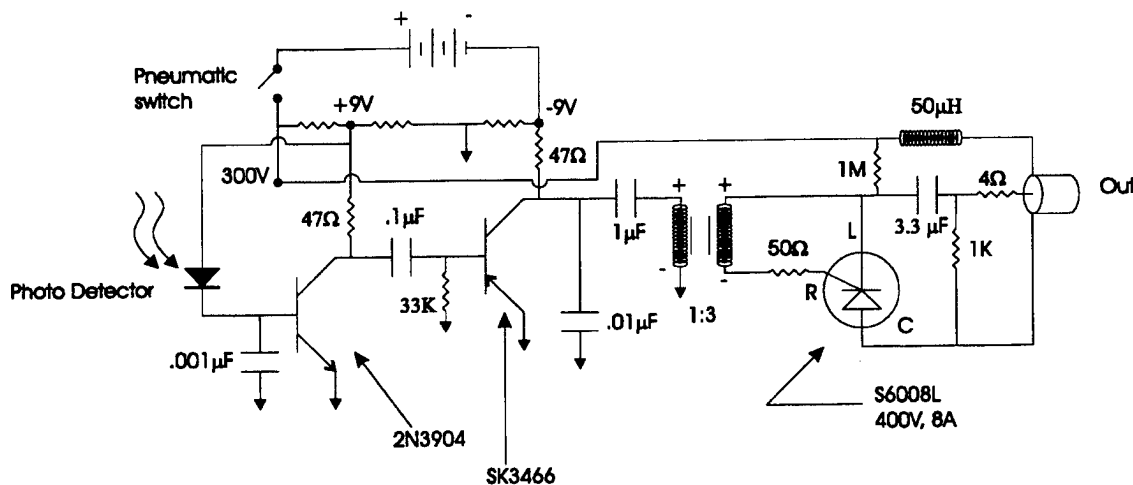


Figure 7. A circuit schematic for the puff valve driver board. This circuit is an optically triggered capacitive discharge that supplies a 300v, 1.8 A, 200 μ s pulse to the valve.

All of the modifications noted above were made within the first 6-9 months of the program. The IP remained essentially unchanged for about 18 months until it became clear that the device was too large to install on Hawk. A series of changes were then made to meet the requirements of the Hawk experiments. None of these modifications had a noticeable impact on the operation of the source from a plasma production standpoint, they were made

to accomidate the installation on Hawk. The first change that was made was the reduction of the outer diameter of the IP to 9.5 cm. This allowed us to install the source inside a Hawk cathode with a 12.7 cm outer diameter. At this time a new puff valve driver was developed. We wanted a small, optically triggered, battery powered discharge circuit that could be mounted *in situ* if the need arose. As a result, the circuit shown in Figure 7 was developed. It couples a light signal to a photo-diode that initiates a sequence of electrical pulses ending in the discharge of a $3.3 \mu\text{F}$ capacitor through the valve coil. A 4Ω resistor is in series with the coil to limits the coil current to safe levels. No noticeable change in the operation of the IP was detected below 600 psig gas pressures. However, for higher pressures, capacitors smaller than $3.3 \mu\text{F}$ did not open the valve properly. An *in situ* mounting system was fabricated for the driver and battery power supply. Although this was not used on Hawk, it was successfully tested at HY-Tech and remains an option for future use.

Section 5

Diagnostics for the Inverse Pinch

This section will describe the diagnostic techniques that were used on the IP plasma to determine various parameters, and monitor its operation. Most of the important results were obtained using a time resolved, He-Ne heterodyne interferometer in a number of different configurations. With this interferometer time dependent electron density information was obtained. A magnetic pick-up loop array and high-speed optical framing photography was also used to gain information on the motion of the current front. Measurements were also conducted at the Naval Research Laboratory, using their ultra-sensitive interferometer, to measure neutral gas distributions emanating from the puff valve/nozzle system of the IP. Finally we will also summarize the results of spectroscopic observation conducted on the hydrogen plasma and the subsequent modeling by Plasma Analyses.

5.1 Rogowski Current Monitor.

A Rogowski coil was constructed to monitor the total current flowing through the IP. For most of the experiments, this monitor was mounted around the quartz insulator inside the SF₆ chamber as shown in Figure 2. The monitor had approximately 40 turns and its output was fed into a 1 ms passive integrator. This coil was calibrated by creating a simple discharge forcing current to flow simultaneously through the IP Rogowski and a factory calibrated T&M Inc. current transformer. The IP mounted Rogowski had a sensitivity of 225 kA/V. Prior to the Hawk experiments, a new monitor was installed inside the spark gap switch. This change was made to avoid having a signal cable inside the vacuum chamber. The new monitor was constructed in a similar fashion and was placed around one of the 12 feed cables so it measured directly 1/12 of the total current.

5.2 Visible Light Framing Camera.

Using a high-speed optical framing camera, the distribution of emitted light was recorded. Figure 8 shows the system that was used. A Kentech model 55 camera with a single imaging lens and neutral density filters was set to view the plasma chordally between the electrode

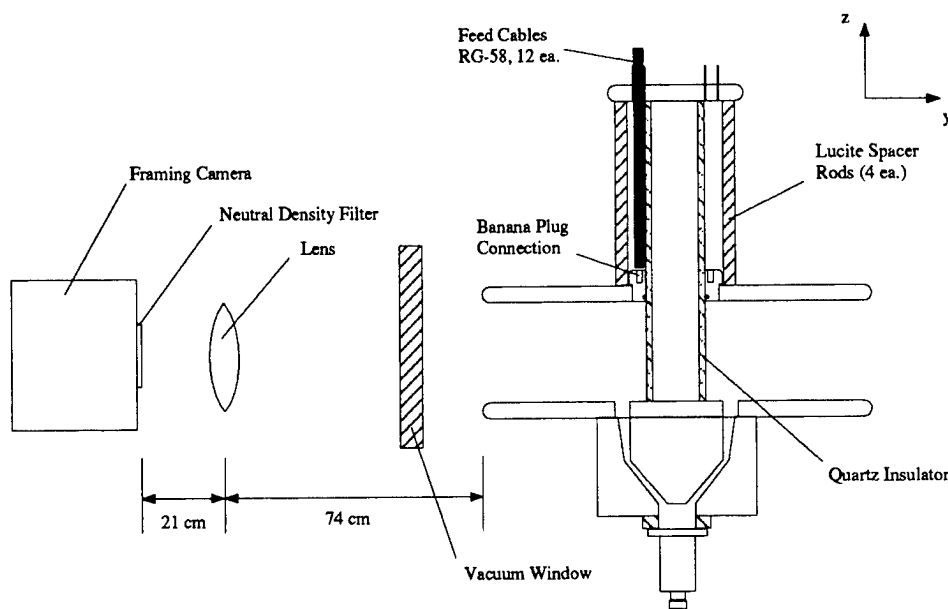


Figure 8. A schematic showing the positions of the framing camera and inverse pinch. The framing camera viewed the plasma chordally and was varied in the x -direction.

plates. The image was reduced by a factor of 3 in the process and frame times of 10 ns were used.

5.3 Magnetic Pick-Up Loops.

An array of magnetic pick-up loops was used to investigate the motion of the current front in the IP. The probe array consisted of six independent loops whose centers were separated by 1 cm and were encased inside a 4 mm outer diameter quartz tube. As configured the loops were 2 mm wide by 4 mm long, with a 6 mm space between each loop. The raw signals obtained from these types of probes produced signals proportional to the time rate of change of the magnetic flux through the loop area, i.e $d(\mathbf{B} \cdot \mathbf{A})/dt$, where \mathbf{B} is the magnetic field and \mathbf{A} is the area of the loop normal. To obtain a signal proportional to the magnetic field, we passively integrated the signal from each loop in the screen room and fed the result directly into an oscilloscope. As a result, the signal we measured was proportional to the strength of the magnetic field. Two arrangements of the loop array was used, and these are both shown in Figure 9. The configuration shown in part (a) was used to determine the velocity of the

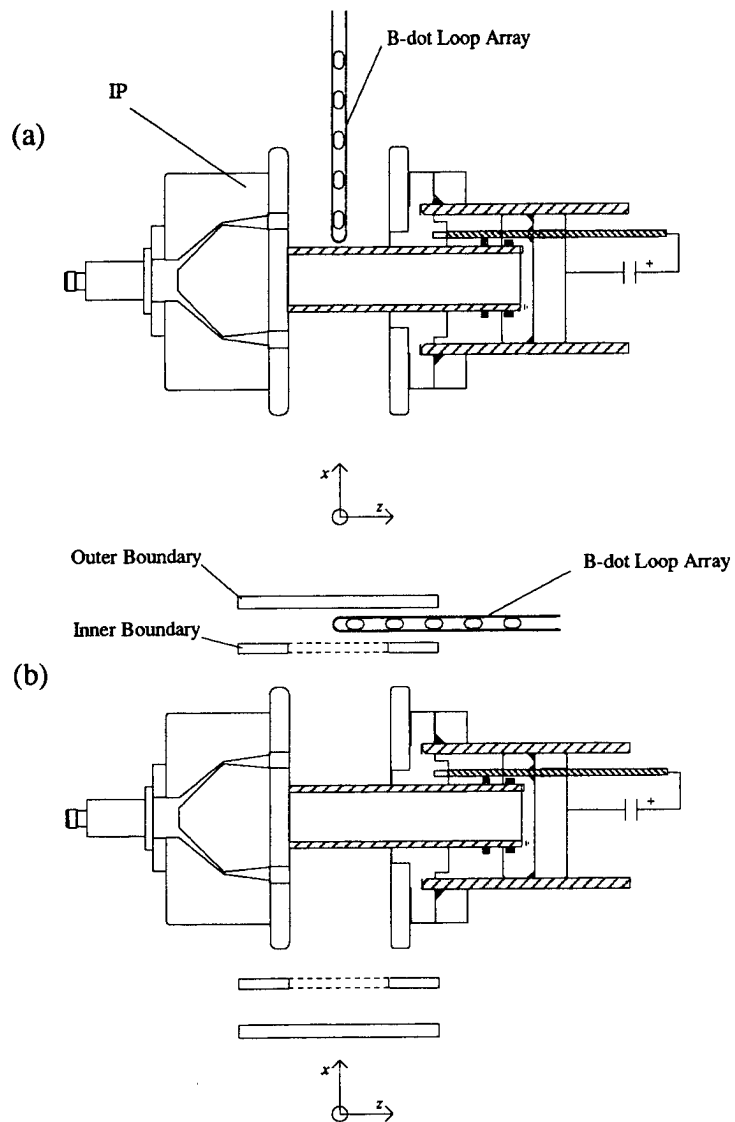


Figure 9. Configurations of the magnetic pick-up loop array that were used. The orientation in (a) was used to determine the expansion velocity of the current front, and (b) was used to investigate the axial expansion of the plasma with the IP mounted insided a "mocked-up POS."

current front between the IP electrodes, and the configuration in part (b) the existence of axially expanding current fronts.

5.4 Time Resolved Heterodyne Interferometer.

A time resolved heterodyne interferometer system, using a He-Ne laser, was frequently used to measure the plasma electron density.[5] With this type of interferometry the scene and reference arms of the interferometer were frequency shifted by 40 MHz using an acousto-optic modulator, or Bragg cell. Upon reconstruction, the interference pattern was modulated at 40 MHz, and a single 40 MHz optical detector was used to detect the light. The signal from the detector was mixed appropriately with the original 40 MHz oscillator to produce two output signals whose ratio was equal to the tangent of the phase difference introduced by the plasma. This diagnostic is shown schematically in Figure 10. Using that system, we were able to achieve a phase resolution of $\pm 1.5^\circ$ by eliminating sources of noise.

Slight alterations in the set-up shown in Figure 10 were used to meet the specific needs of a particular measurement. For instance, in cases where spatial resolution was important, the probe (or scene) beam was focused using a long focal length lens to achieve a 1 mm spatial resolution. Without such a lens the spatial resolution was approximately 3 mm. In another case, a two channel interferometer was required to measure the electron density at two locations simultaneously. For the two channel interferometer, the laser beam was split into two probe beams and two reference beams with each pair functioning as an independent interferometer. Two separate detectors and mixing networks were used to measure the phases from each channel. A schematic of the two channel interferometer is shown in Figure 11.

Figure 12 shows the three most important configurations of the basic interferometer system that we used. In part (a), the chordal line-of-sight (LOS) configuration is shown. If we let the axis of the IP define the z -axis of our coordinate system, then this LOS has the laser beam propagating parallel to the x -axis at a constant y position. This configuration was most often used to measure the axial profile of the plasma which could be accomplished by varying the z position of the laser beam on successive shots. It should be pointed out, that with this LOS, the average plasma density is not measured because the laser samples different radial locations during its path. To obtain the actual density from measurements with this LOS, an Abel inversion must be performed.[6] However, even without an Abel inversion, relative measurements are possible. In part (b), the axial line-of-sight interferometer is shown. In this case the beam travels parallel to the z -axis. This LOS was used to measure radial distributions and radial expansion velocities of the IP plasma. Note that in this case the laser beam sampled the plasma at a constant radial location. Therefore, averaged plasma

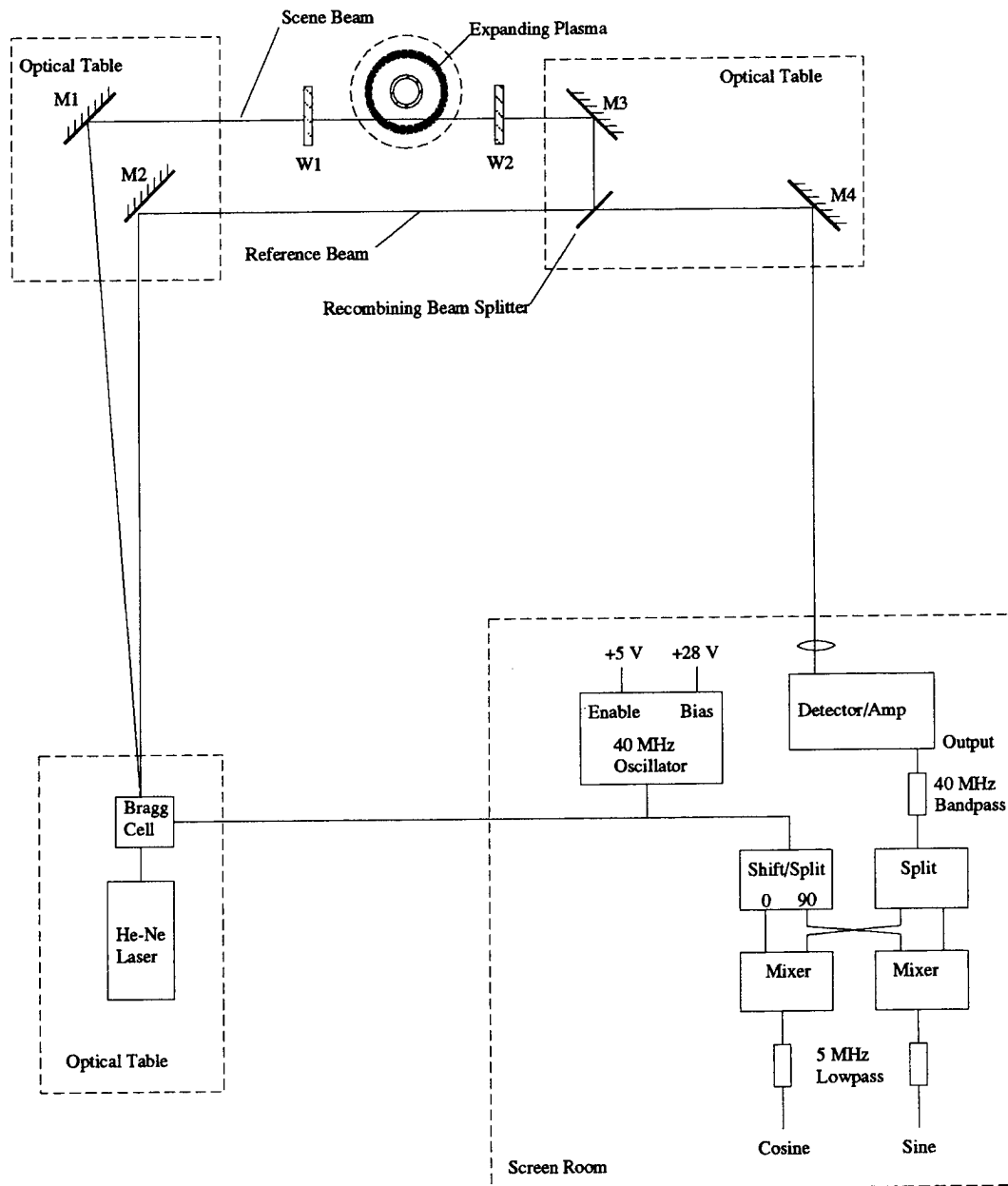


Figure 10. A schematic of the phase sensitive He-Ne interferometer that was used to perform the electron density measurements. A similar configuration employing 2 optical tables was also used. For each shot, the sine and cosine signals were recorded on an oscilloscope and processed after the shot to determine the phase as a function of time.

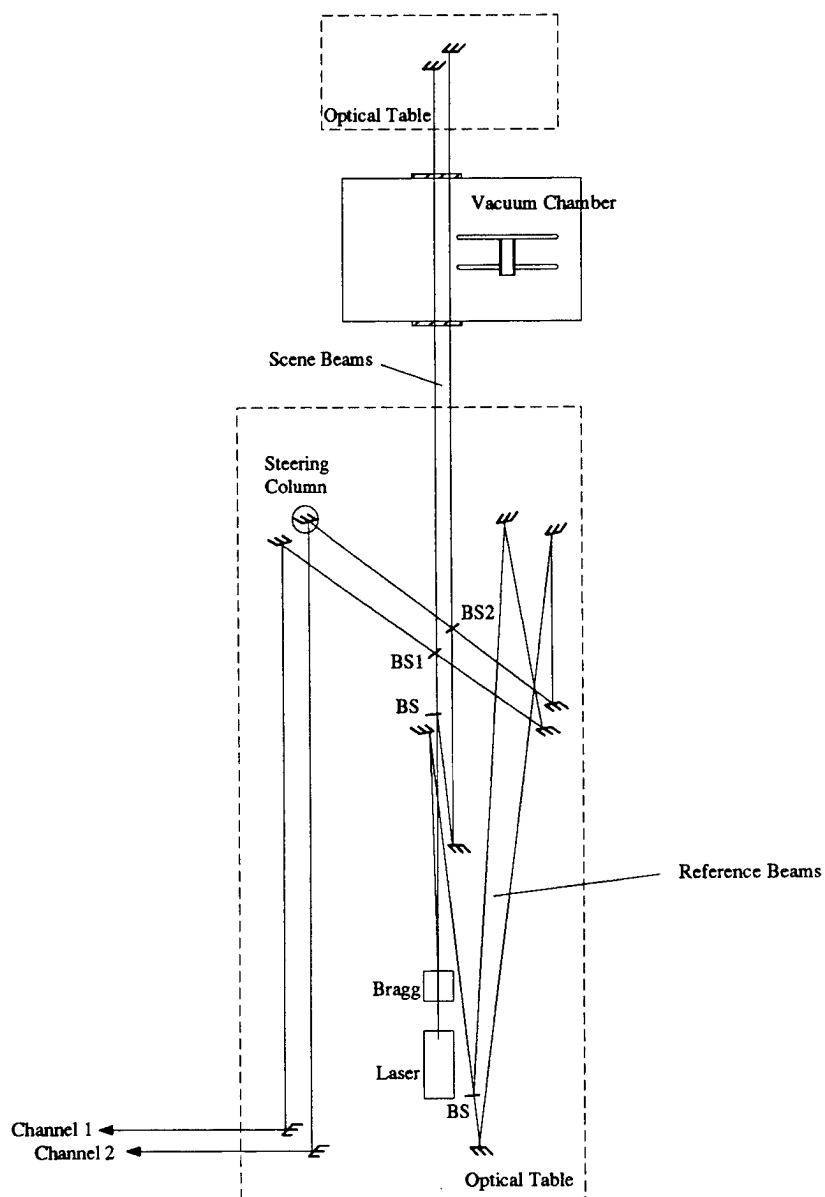


Figure 11. A schematic of the two channel interferometer. The light signals from each channel were fed into detectors located in a shielded room and recorded in exactly the same manner as the single channel interferometer shown in the previous figure.

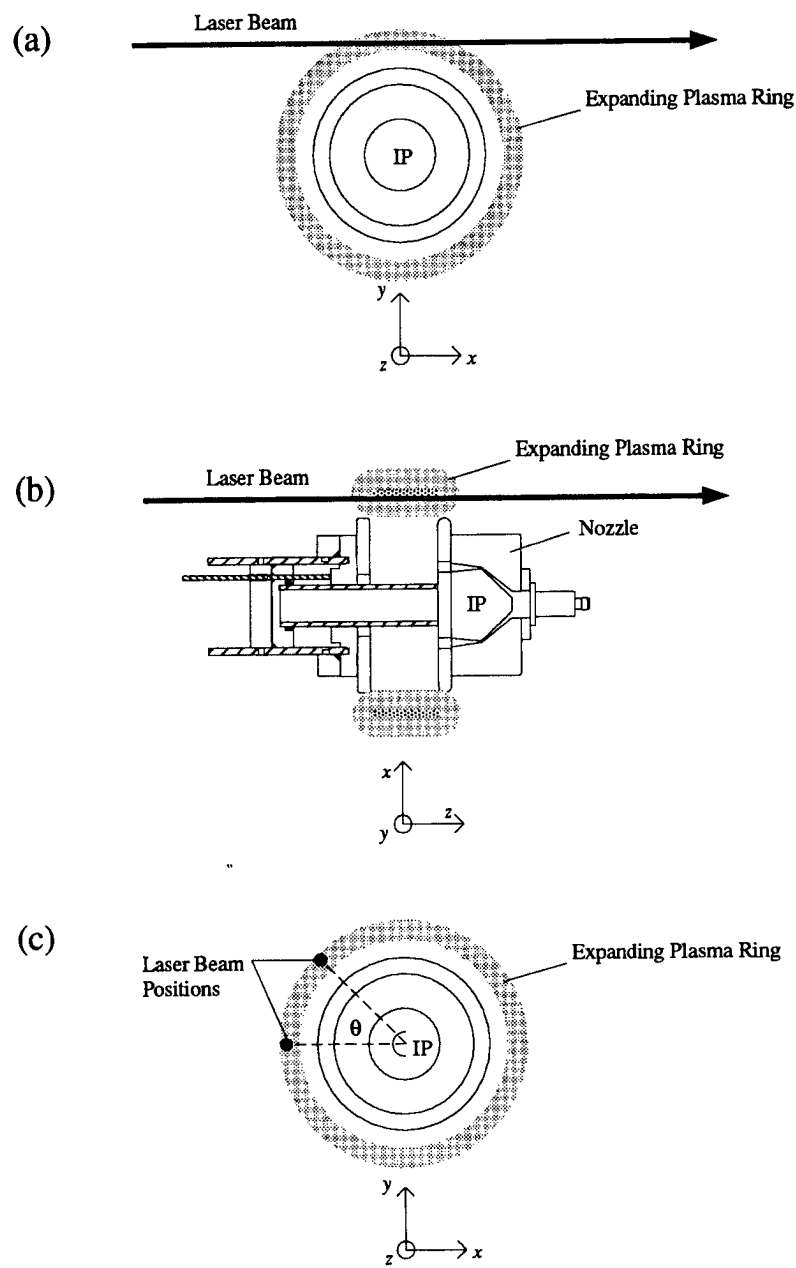


Figure 12. Various interferometric configurations that were used. Part (a) shows the interferometer viewing the plasma chordally, (b) viewing the plasma axially, and (c) shows the two channel interferometer with the beams separated by angle θ .

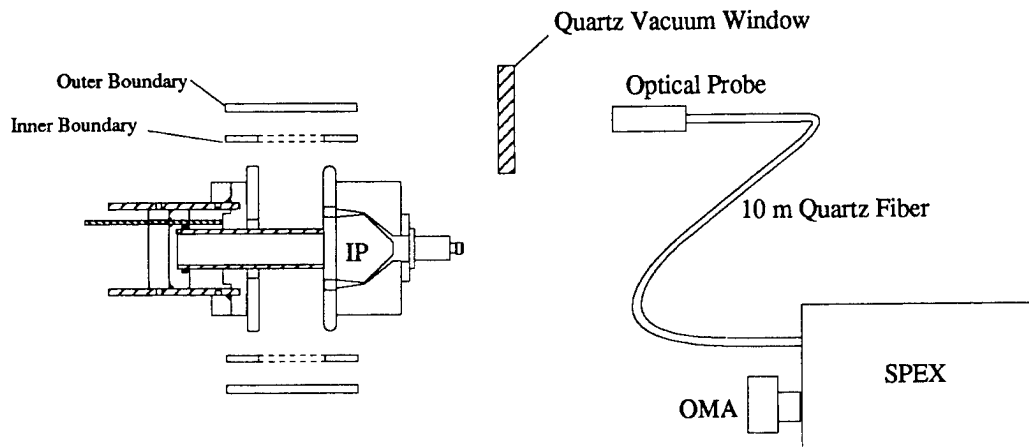


Figure 13. A schematic showing the apparatus for observing optical spectra from the IP. The probe viewed the gap between the inner and outer boundaries surrounding the IP along an axial line of sight. The position could be varied radially by moving the probe.

densities as a function of radius were obtained directly from the phase signal. In part (c) the orientation of the two channel interferometer is shown. In this case both beams were set up to view the plasma axially with each beam the same distance from the z -axis. For these measurements the angle between the beams in the x - y plane, θ , could be varied.

5.5 Two Wavelength Interferometry.

We used the ultra-sensitive, two-wavelength interferometer at the Naval Research Laboratory to make measurements on the neutral gas distribution produced by the IP puff valve/nozzle. We will not include details on this diagnostic as they are published,[7] but it should be noted that the measurements we conducted were not possible with apparatus at HY-Tech. Phase shifts due to neutral gas are roughly two orders of magnitude less than an equivalent number of electrons and require a much more sensitive device given the gas densities produced by the IP. The interferometer at NRL was approximately 10^4 times more sensitive than our heterodyne system. When conducting these measurements we used a single beam directed chordally and were most interested in the gas distribution between the electrode plates inside the IP.

5.6 Spectroscopic Measurements.

Visible light spectroscopy was performed on IP plasmas in a mock-up POS arrangement as shown in Figure 13. For these observations we used an optical probe consisting of a 12.5 mm diameter fused silica lens with a 75 mm focal length that was set to collect light axially. The output of the lens was fed into a 10 m, 100 μ m quartz fiber that carried the light into a spectrometer located in a screened room. The spectrometers used were either a 3/4 m SPEX or a 1/2 m McPherson with an OMA detector at the output plane. This probe assembly had a spatial resolution that was approximately 1 mm and its position could be varied radially. Most of the spectroscopic measurements were gathered using a hydrogen plasma to help determine the electron temperature and the percentage of neutrals that may exist in the initial plasma for POS shots.

Section 6

Experimental Measurements

In this section we will detail the results of experimental measurements performed on the IP source. We include results of the neutral gas measurements, measurements on the expanding plasma shell, the exhaust plasma, and measurements performed in a POS-like environment. By a POS-like environment we mean a configuration where the IP is placed inside two co-axial cylinders where the inner cylinder is semi-transparent, as it would be in a real POS. Illustrations of this arrangement were displayed in the previous section. Most of the data was taken using H and Ar plasmas since these represent extremes in the available gases. The electrical breakdown properties of these two gases are also favorable leading to relatively consistent IP operation. Because of the mass dependence associated with the conduction phase of a POS, we were interested in IP/H shots with a high pressure gas puff and relatively large electron densities ($600\text{-}800$ psig, $n_e > 5 \times 10^{15}\text{cm}^{-3}$). The interesting operating regime for IP/Ar shots was $50\text{-}100$ psig and $n_e \sim 1 \times 10^{15}\text{cm}^{-3}$.

6.1 Neutral Gas Measurements.

Measurements of the neutral gas distribution was performed on the IP without forming plasma. The purpose of these measurements was to investigate the dynamics of the gas puff on the time scales of interest. Typically, during operation of the IP, the gas valve was discharged $350\text{-}700$ μs before the application of high voltage and current. This delay range depended on the type of gas, with the longer delays applicable to the heavier gases such as Ar. For H_2 gas, delays in the $350\text{-}400$ μs range with $600\text{-}800$ psig puffs were of particular interest because they were used on the Hawk experiments. The gas distribution under these conditions was investigated on a test stand at NRL using the ultra-sensitive interferometer. The IP was arranged so the interferometer beam traversed a chordal line-of-sight through the inter electrode region of the IP, and the time evolution of the phase at that position was recorded. Defining $z = 0$ as the axial position of the IP anode (electrode plate with puff valve/nozzle), we made measurements at three axial positions while varying the probe laser beam radially. Figure 14 shows the beam locations during the puffed gas experiments. A number of observation (3-5) were recorded at each location, averaged, and uncertainties

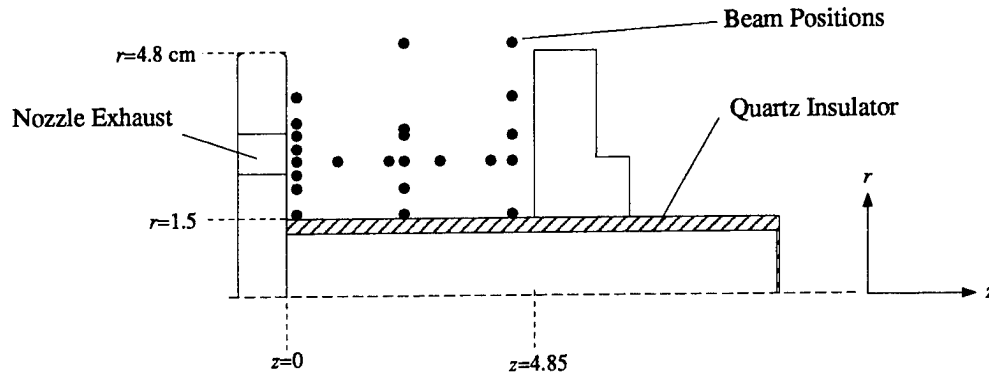


Figure 14. An illustration showing the laser beam positions used to measure the neutral gas distribution produced by the IP puff valve/nozzle system. A cross-section of the $r - z$ plane is shown.

calculated. For the H_2 and Ar gases values for the index of refraction tabulated in the CRC Handbook of Chemistry and Physics were used to convert the phase shift to line integrated density. Then for each axial position, the line integrated density data was Abel inverted to obtain the radial distribution of the gas density as a function of time. The result of the H_2 measurements at 800 psig are shown in Figures 15 and 16. Figure 15 shows the measured gas densities as a function of radius for times of interest where $r = 1.5$ cm is the surface of the quartz insulator. Parts (a),(b), and (c) of this figure show the measurement at three different axial positions of 0.2, 2.3, and 4.4 cm respectively where the error bars reflect the propagation of uncertainties through the Abel inversion. These plots show that the gas spreads out very quickly after exiting the nozzle. Figure 16 shows the same data in Figure 15 displayed as the mass per unit length as a function of time for the three different axial locations. This data was obtained by performing a radial integral as a function of time at each respective z location.

6.2 Measurements on the Expanding Plasma Shell.

Numerous measurements were performed on the expanding plasma shell, prior to ejection from the source, to investigate the dynamics of IP operation and the formation of plasma. Most of these measurements were conducted during the early stages of the program using an IP with the largest diameter electrodes (20.3 cm).

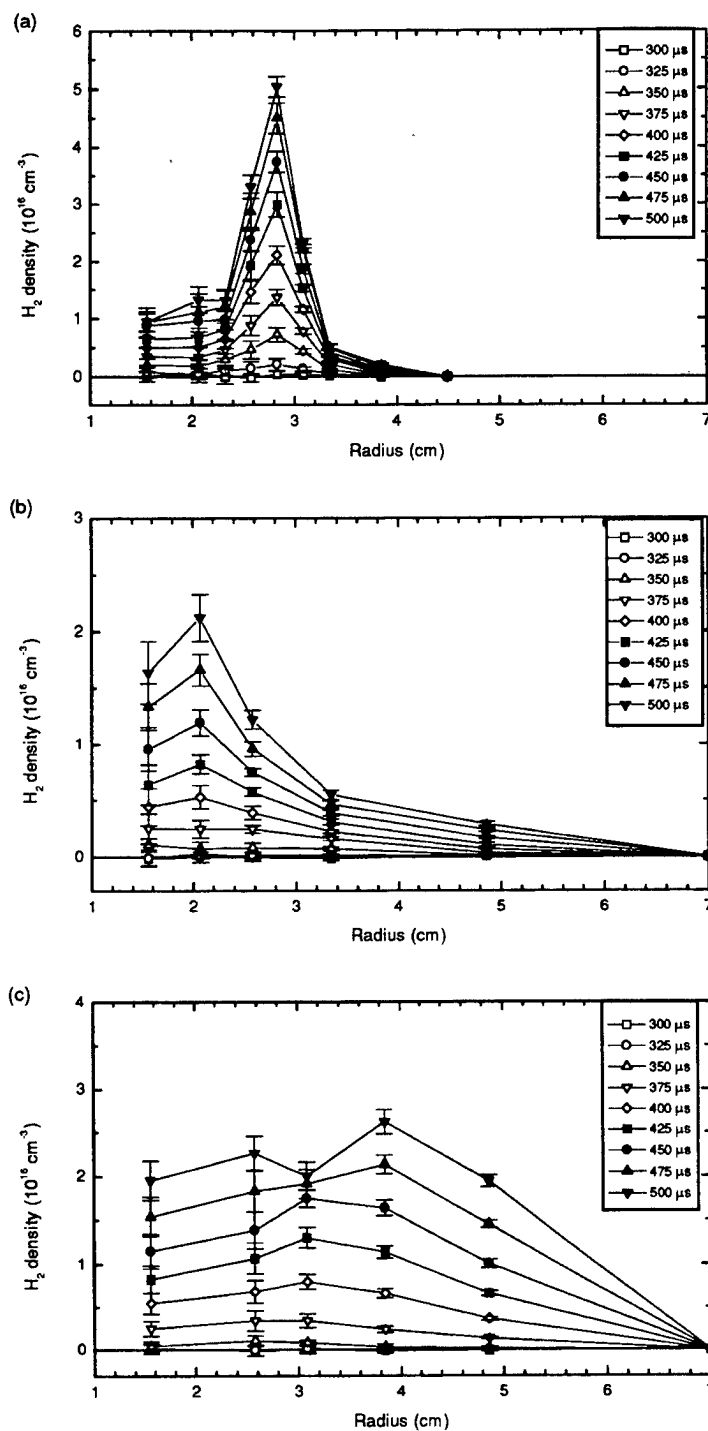


Figure 15. The H_2 gas density as a function of radius as determined from an Abel inversion is plotted. Each plot shows the density at various times with (a) corresponding to $z = 0.2 \text{ cm}$, (b) to $z = 2.3 \text{ cm}$, and (c) to $z = 4.4 \text{ cm}$. The puff valve pressure was 800 psig and $t = 0$ is defined when the valve is pulsed.

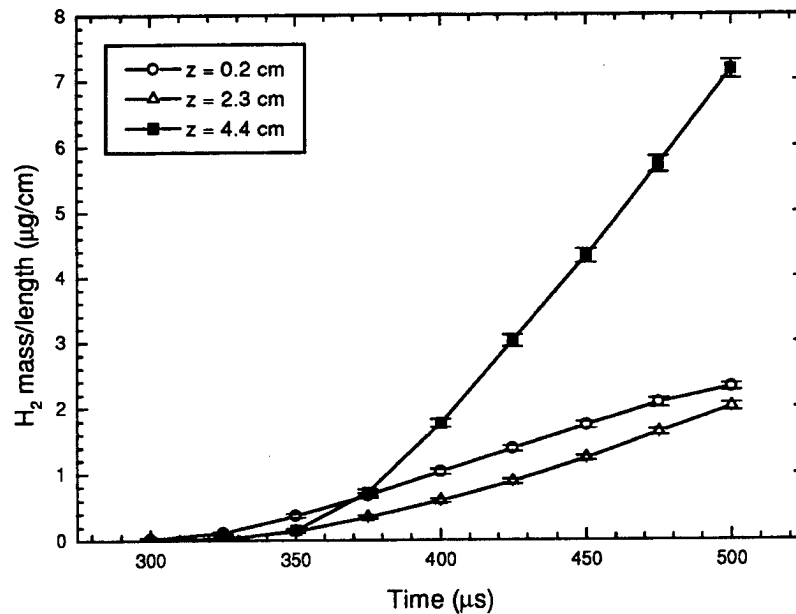


Figure 16. The mass per unit length in $\mu\text{g}/\text{cm}$ of H_2 as a function of time at various z positions in the inter-electrode region of the IP. The puff valve pressure was 800 psig and $t = 0$ is defined when the valve is pulsed. These values were calculated from the density measurements shown in Figure 15.

6.2.1 Visible Light Framing Photography.

Figure 17 shows a sequence of visible light photos obtained from a framing camera that viewed the plasma chordally as shown in Figure 8. For the sequence shown in the figure the IP was operated with H_2 gas and the shutter speed of the camera was set to 10 ns. We observed that early in the discharge light was emitted from the quartz insulator and propagated radially outward as one would expect. This verifies that the breakdown was initiated at, or very close to, the quartz insulator. Later in time we can also see that the luminous front is bowed indicating a drag imparted to the shell by the electrode surface.

6.2.2 Magnetic Pick-up Loops.

We also inserted a magnetic pick-up loop array as shown in Figure 9(a) to determine the speed and position of the magnetic front propagating radially outward between the electrode plates. The array was positioned so it was in the axial center between the IP electrode plates. Figure 18 shows the data and deduced radial position and velocity from those measurements

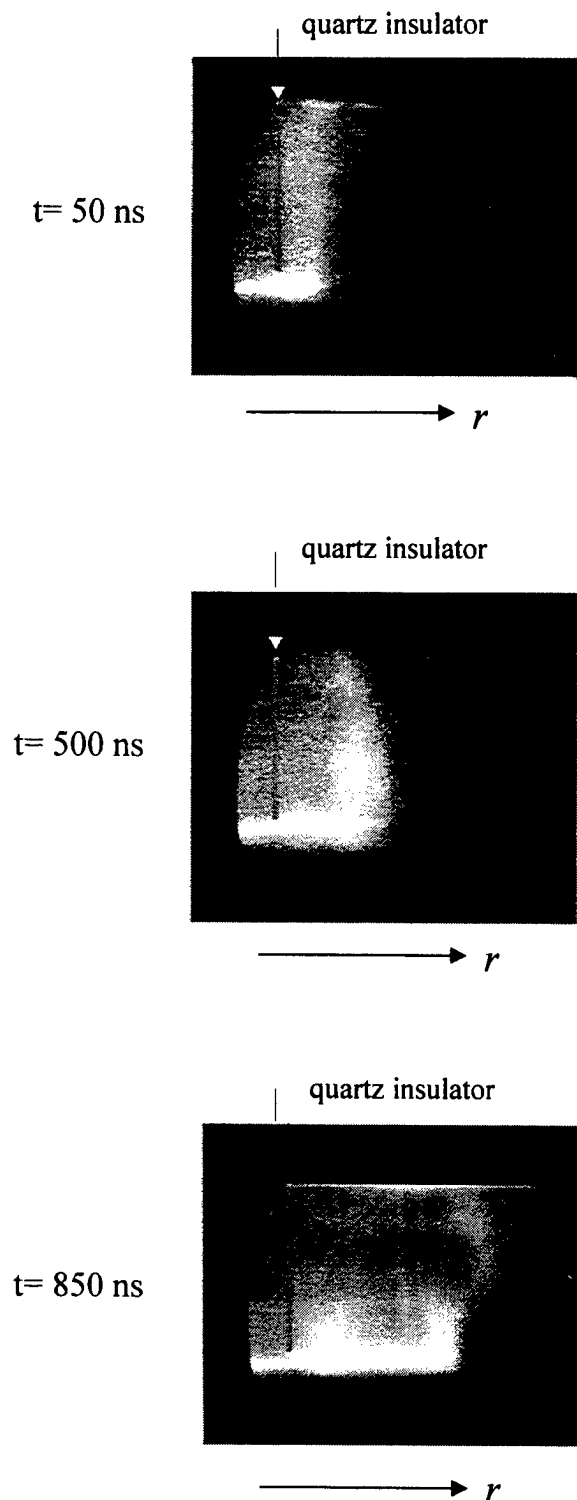


Figure 17. A sequence of photos that shows a luminous front propagating radially outward. The times are referenced to the start of current flow in the IP and show that the breakdown starts at the quartz insulator. The radial location of the quartz tube is indicated.

at two different puff valve delays. Note that the puff valve driver was different than the one used later on experiments at NRL and HY-Tech. Part (a) is the raw data that shows the current in the inverse pinch as well as the relative strength of the magnetic field as determined from each probe. The probe locations varied from a radius of 3 to 11 cm for probes *bd1* – *bd9* respectively. One can see that by $0.5 \mu\text{s}$ into the discharge, the magnetic piston has passed the location of *bd1* and has not reached the location of *bd2*. Defining the half maximum of each probe signal as the location of the current front, the data shown in part (b) was determined which shows the radial position of the piston as a function of time keeping in mind that $r = 10 \text{ cm}$ is the edge of the electrodes. In part (c) the velocity of the magnetic piston is shown obtained from the time derivative of the plot in part (b).

6.2.3 Chordal Line-of-Sight Interferometry.

Chordal line-of-sight time resolved heterodyne interferometry was also performed to directly observe the radially expanding plasma between the electrode plates. The arrangement of the interferometer and the inverse pinch for this set of measurements was shown in Figure 12(a). In this instance the probe laser beam was 1 mm in diameter and directed along a chord through the axial center of the IP electrodes. A scale perpendicular to the beam direction (y -axis) was used to indicate the position of the beam. We were able to view the plasma from just off the surface of the quartz insulator ($y=1.5 \text{ cm}$) to near the end of the IP electrodes at $y=10 \text{ cm}$. Typical interferometer signals from 4 IP/ H_2 and IP/Ar shots are shown in Figure 19 where $t=0$ defines the start of current flow in the IP. In general, 4-5 shots were performed at each beam position producing an average and standard deviation for each y location. The data was then Abel inverted to produce the electron density as a function of radius. Results of the Abel inversion for IP/ H_2 , IP/Ne, and IP/Ar data are shown in Figure 20 for a single time referenced from the start of current flow in the IP. In both cases we observe a narrow radial region where the plasma density is non-zero, and essentially zero density (to within experimental error) for other radii. By analyzing the data as a function of time, the position and velocity of the plasma can be determined. These results are shown in Figure 21 for all three gases. It is important to note that the size of the gas puff (200 psig) were significantly smaller for these IP/ H_2 shots compared to later experiments performed on Hawk. As a result the velocities are significantly higher in this case.

6.3 Measurements on the Exhaust Plasma.

A series of measurements was performed on the exhaust plasma, or the plasma that is ejected by the IP. We were primarily interested in the ejected velocity and ejection time of

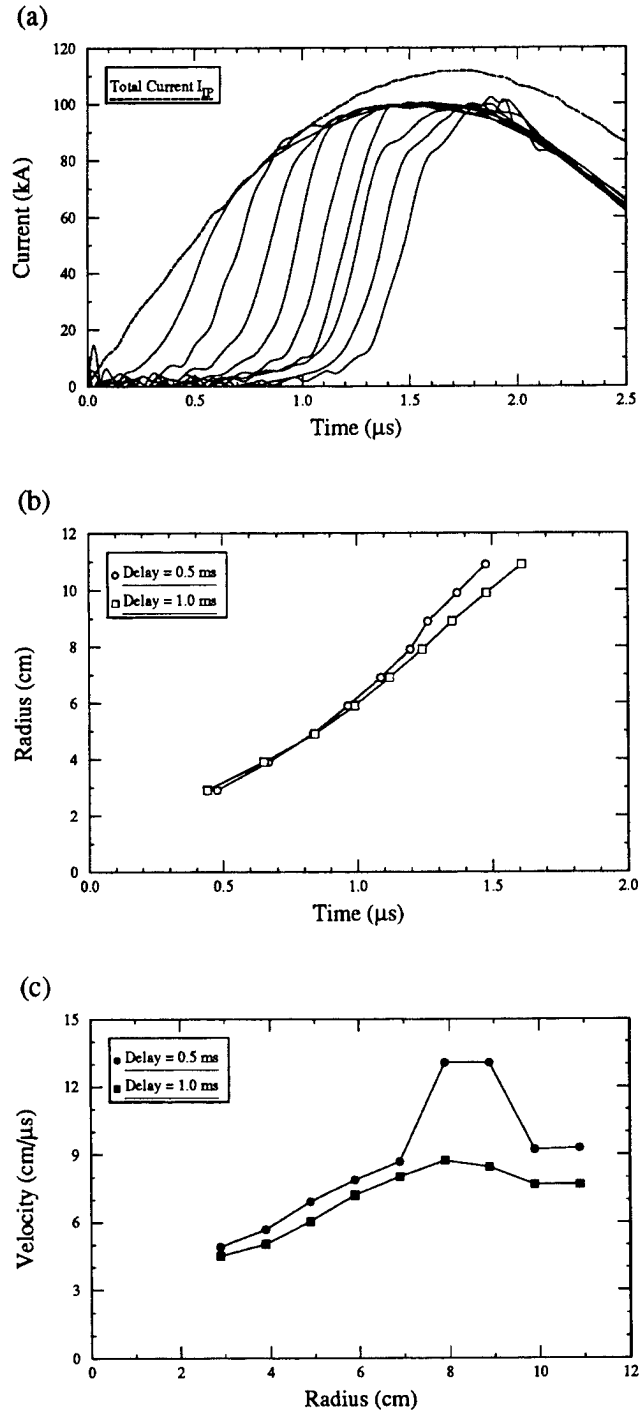


Figure 18. Results from the magnetic pick-up loop analysis. Part (a) shows the raw data with a 0.5 ms puff valve delay, shown are signals from *bd1-bd9* and an IP current trace. The loop signals were arbitrarily scaled. Part (b) shows the radius of the current sheet as a function of time, and (c) shows the velocity of the current sheet as a function of radius for puff valve delays of 0.5 ms and 1.0 ms.

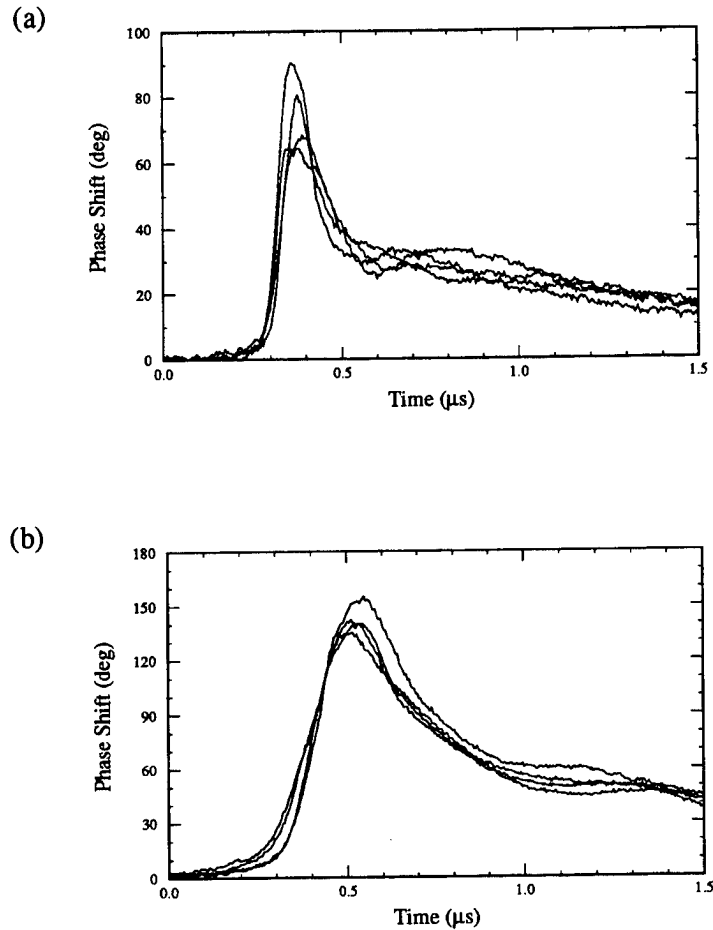


Figure 19. Examples of raw interferometer signals showing the phase shift as a function of time for, (a) four H_2 shots and (b) four Ar shots.

the plasma, as well as the general characteristics of the plasma ring. The results were then compared to a simple 1D snowplow model which allowed us to predict the ionization state of Ar. In this section we will show data that used the IP with 12.7 cm diameter electrode plates.

6.3.1 Exhaust Measurements Using Heterodyne Interferometry.

Using the interferometric configuration shown in Figure 12(b), where the laser beam is directed axially, we measured some basic parameters of the ejected plasma from the IP for H_2 , Ne, CH_4 , and Ar gases. A typical interferometer signal using this line-of-sight is shown in Figure 22. The shape of the signal indicates that the plasma is accurately described as

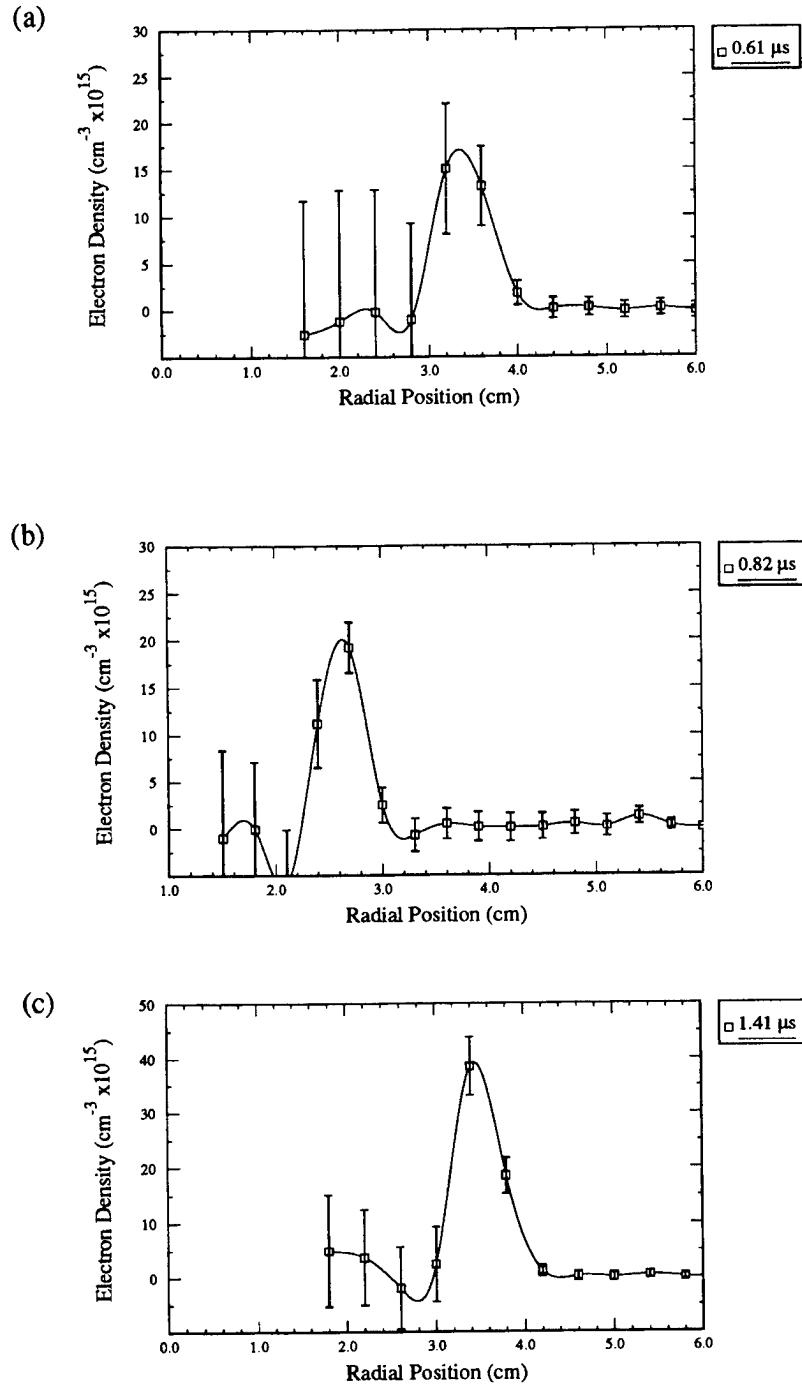


Figure 20. Abel inverted density profiles of the plasma shell as determined from the chordal interferometry measurements. Plotted are the electron densities vs. radial position for (a) hydrogen at 0.61 μs after the discharge began, (b) Ne at 0.82 μs and (c) Ar at 1.41 μs .

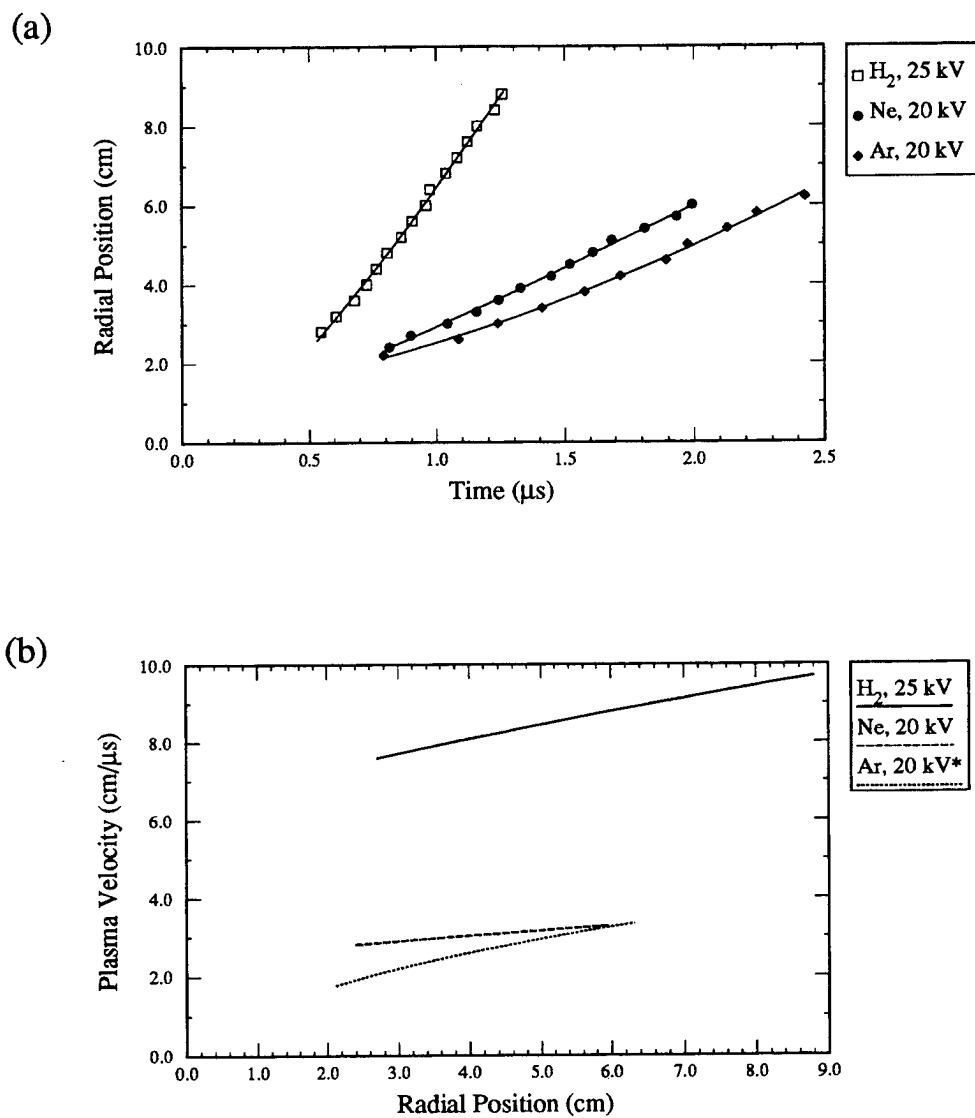


Figure 21. The radial position of the plasma shell as a function of time is shown in part (a) for various gases. The velocity of the plasma shell as a function of radial position is plotted in (b). Note that a different nozzle design was used for the Ar data.

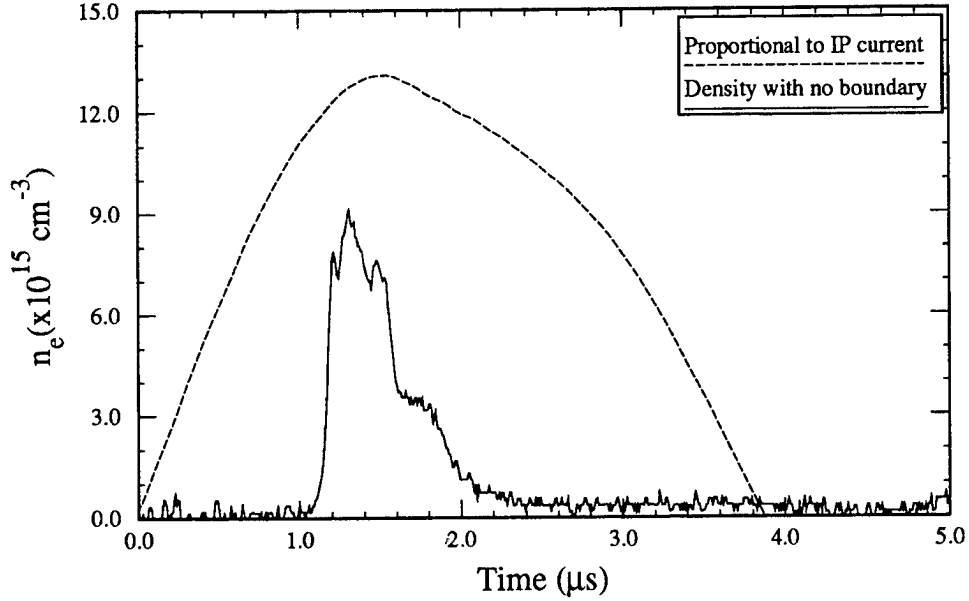


Figure 22. The plasma density as a function of time for the case where the IP was operated without a boundary. In this case H_2 gas was used with an axial line-of-sight interferometer positioned a few mm from the edge of the IP electrode.

a plasma ring that expands radially. Thus we observe that once the ring has passed by the laser beam the phase shift becomes very small. By recording data from 4 shots for each gas at a number of radial positions, we can determine some basic parameters for the exhaust plasma. We will define the arrival time of the plasma at the laser beam position as, $\langle t \rangle$, by performing the following integral on the recorded phase,

$$\langle t \rangle = \frac{\int t \phi(t) dt}{\int \phi(t) dt}, \quad (1)$$

where $\phi(t)$ is the measured phase shift as a function of time. Further we can define the ejection time of the plasma as the value of $\langle t \rangle$ when the laser beam was positioned just off the edge of the electrode plates at $r=6.35$ cm. The average velocity of the plasma ring, $\langle v \rangle$, was determined by calculating $\langle t \rangle$ for a number of beam positions (4) and fitting the data to a straight line. We also calculated the total number of ejected electrons, N_e , by using $\langle v \rangle$ and integrating the recorded phase as follows,

$$N_e = (2\pi r_{laser}) \langle v \rangle C \int \phi(t) dt, \quad (2)$$

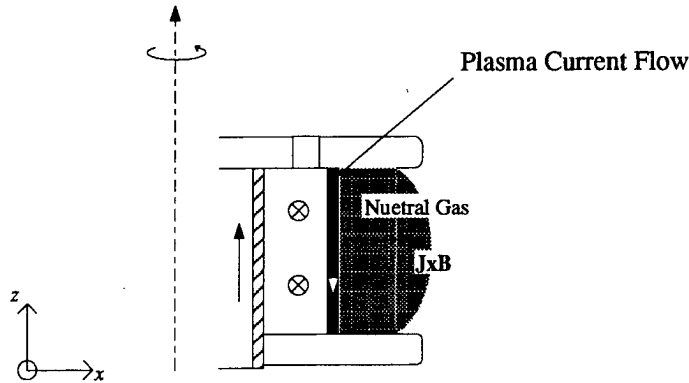


Figure 23. An illustration of a 1D snowplow.

where r_{laser} is the radial position of the laser beam and $C = 9.72 \times 10^{14} \text{cm}^{-2} \text{deg}^{-1}$, converts the phase shift in degrees to the line integrated electron density. Results of these calculations for the various gases will be displayed in the next section.

6.3.2 Snowplow Model for the IP.

We completed a calculation that modeled the operation of the IP up to the ejection of the plasma. This was done using a simple 1D snowplow model to describe the motion of the current front between the IP electrodes. The basic assumption of this model is that an infinitely thin current front (or shell) is accelerated radially outward by the $\mathbf{J} \times \mathbf{B}$ force as it sweeps up and ionizes all the neutral gas in its path. At the start of current flow in the IP, a finite amount of neutral gas is present between the electrodes as a result of a prior puff valve discharge. Therefore, as the current shell moves radially out and sweeps the gas, its mass increases in accordance with the initial mass density of neutral gas. The differential equations that govern the motion of the current shell were numerically integrated to predict the ejection time and velocity of the plasma using the total mass of the neutral gas as variable parameter, and assuming an initial distribution for this gas. The calculated result was then compared to measurements of the ejection time and velocity to determine the plasma mass. With knowledge of the plasma mass from the simulation, and the total number of electrons from the experimental measurements, we can predict the average ionization level of the plasma. Since the ionization level for hydrogen must be +1, the hydrogen case was used to test the accuracy of this method.

Figure 23 illustrates the snowplow process. The current shell experiences a force directed

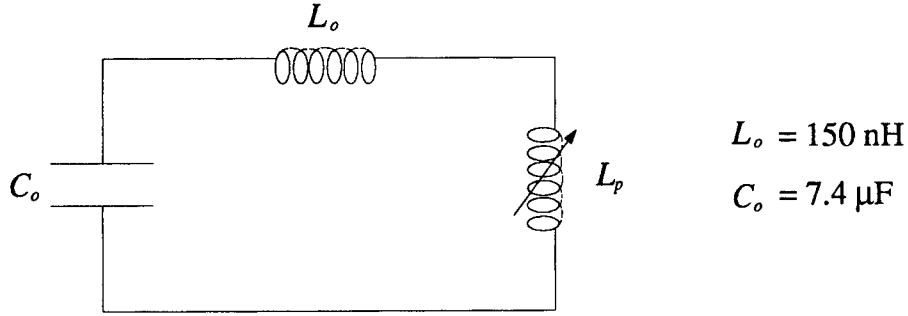


Figure 24. The equivalent electrical circuit for the inverse pinch where the pinch is modeled as a variable inductor.

radially outward due to $\mathbf{J} \times \mathbf{B}$. The motion of the shell is therefore described by the following differential equation,

$$\frac{d}{dt}(M(r)v) = \frac{\mu_o I^2(t)}{4\pi r(t)}, \quad (3)$$

where $v(t)$ is the radial velocity of the shell, $r(t)$ is the radial position of the shell, $I(t)$ is the shell current, and $M(r)$ is the mass/length of the shell which is given by the following,

$$M(r) = \int_{r_o}^r 2\pi r' \rho(r') dr' \quad (4)$$

where $\rho(r)$ is the mass density of the neutral gas and r_o the quartz tube radius. The current can be obtained from the circuit model shown in Figure 24 where C_o is the bank capacitance, L_o the fixed inductance, and $L_p(r)$ the variable inductance portion of the inverse pinch. The inductance of the IP varies with the position of the current shell according to the following equation,

$$L_p(r) = \frac{\mu_o l}{2\pi} \ln\left[\frac{r(t)}{r_o}\right], \quad (5)$$

where l is the axial distance between the IP electrodes. The differential equation for the current is,

$$\frac{d^2}{dt^2}[(L_o + L_p(r))I(t)] + \frac{I(t)}{C_o} = 0. \quad (6)$$

Equations (6.3) and (6.6) form a set of coupled, nonlinear differential equations that were solved numerically. However, we needed a distribution for the neutral gas to solve

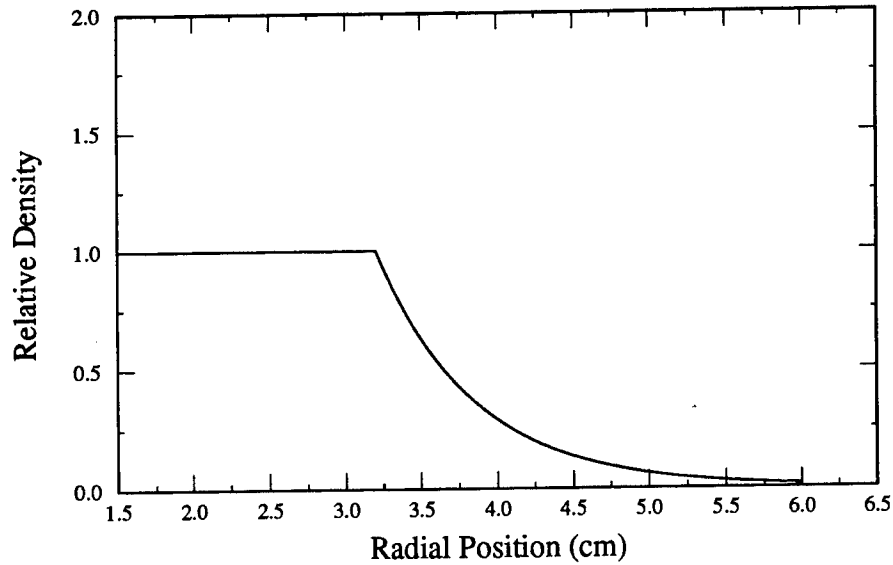


Figure 25. The neutral gas density function that was used for the 1D snowplow calculation. The calculation was not sensitive to the details of this distribution.

these equations. Figure 25 shows the distribution that we used. It has a constant gas density from the edge of the quartz tube at 1.5 cm up to the outer nozzle radius at 3.2 cm, and then an exponential decay. We will also use the following parameters for the calculation, $r_o=1.5$ cm, $L_o=150$ nH, and $C_o=7.4$ μ F. The calculation will be stopped when $r=6.35$ cm, which is the edge of the IP electrode plates. At that point, the time (ie. ejection time) and velocity of the front will be recorded. Calculations were performed while varying the total mass/length of neutral gas and the results are shown in Figure 26. The mass of the neutral gas was varied by using a simple multiplicative factor for the gas distribution shown in Figure 25. Figure 26 shows that the results of the calculation were sensitive to the total mass of the neutral gas. By trying different neutral gas distributions with the same total mass we found that the calculation was insensitive to the details of the distribution.

For IP discharges with H, CH₄, Ne, and Ar the ejection time, velocity, and total number of electrons exiting the device were measured using the heterodyne interferometer as previously described. These results are shown in Table 1. For the hydrogen case we can also calculate the total mass from the total number of electrons assuming that the plasma is fully ionized. In Figure 26 we have added a data point that corresponds to the data measured for hydrogen. For the curve in Figure 26(a) this data point matches extremely well with the calculated

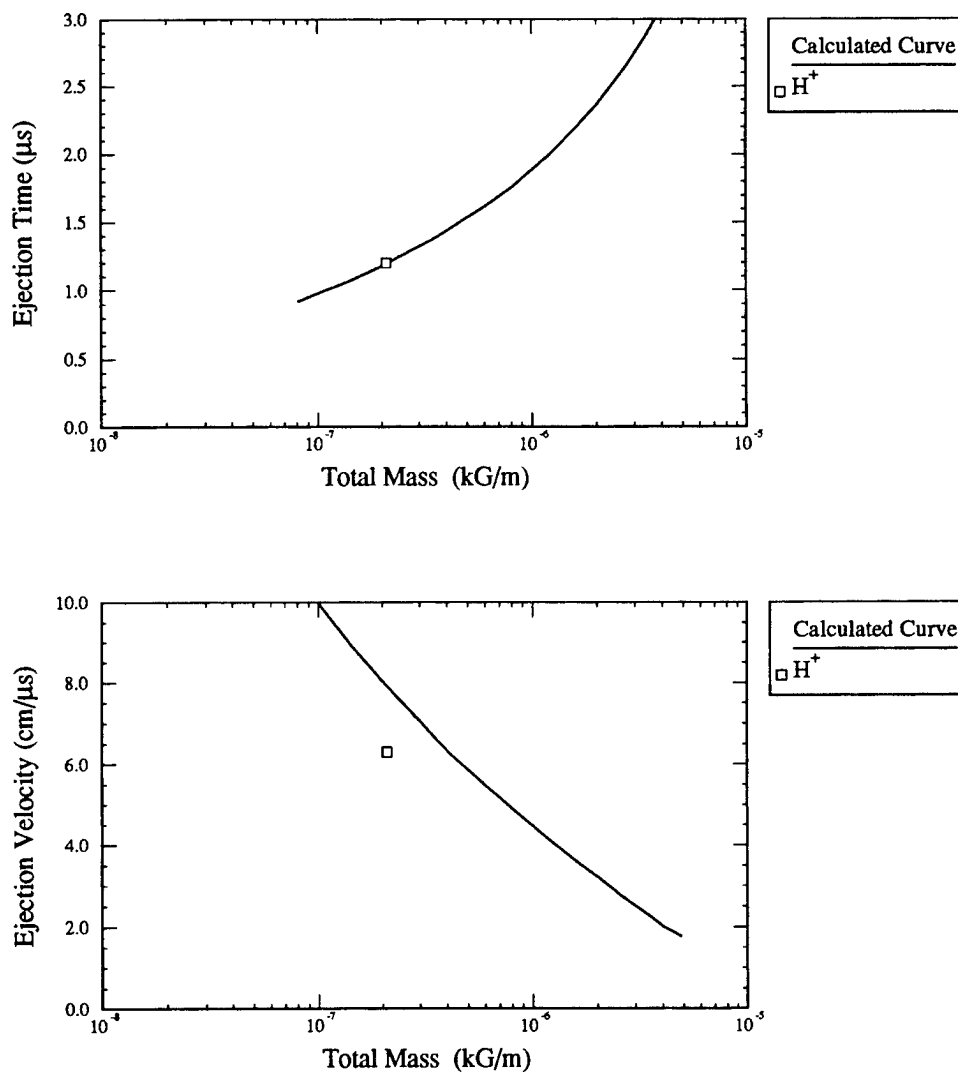


Figure 26. Results of the 1D snowplow calculation. In part (a) the calculated ejection time vs. the total mass per unit length of the neutral gas is plotted. In part (b) the calculated ejection velocity vs. the total mass per unit length of neutral gas is plotted. In each plot a single data point corresponding to the measurements on hydrogen gas is also shown.

Table 1. Key experimental and calculated results for the IP with various gases. Listed for each gas are the experimentally measured plasma ejection time (τ_e), ejection velocity (v_e), average number of ejected electrons (\bar{N}_e), and the predicted number of electrons per molecule (N_m) obtained from the 1D snowplow calculation.

Gas	Experimental Measurements			Calculation
	τ_e (μs)	v_e (cm/ μs)	\bar{N}_e ($\times 10^{18}$)	N_m
H ₂	1.2	6.2	6.3	1.9
CH ₄	1.8	4.0	6.2	3.8
Ne	2.1	3.9	4.5	2.1
Ar	2.5	3.3	3.3	1.9

result for the ejection time vs. total mass/length, however, it is a rather poor match for the calculation of the ejected velocity as shown in part (b). This may be due to the fact that the ejection time is directly obtained from measurements at one location, while the velocity must be determined from measurements at a number of radial locations and will involve more error. Using the data for all the gases, we determined the number of electrons per injected gas molecule, so the total mass matches the snowplow calculation. The last column in Table 1 shows this result. For hydrogen, the snowplow calculation predicts an ionization level very close to +1 (ie. two electrons per molecule), while both neon and argon are very close to +2. The methane result is very interesting as it predicts that only about 4 electrons are expected per molecule. This implies that some of the methane is not completely broken down, i.e. some of it would exist as molecular ions such as CH⁺, CH₂⁺, etc. This very simple 1D snowplow model has given us a reasonable estimate of the ejected plasma mass, and ionization state, by comparing the calculated result to the measured ejection time of the plasma. The calculation is insensitive to the details of the neutral gas distribution, but very sensitive to the total mass of the gas between the electrodes.

6.4 Measurements in a POS-like Configuration.

In this section we will summarize the results of measurements that were performed on the IP using interferometry and magnetic pick-up loops. We will concentrate on those results that have a direct bearing on the effectiveness of the IP as a plasma source for opening switches. In each of these cases, the data that we will present was taken with the IP placed inside a "mocked-up" POS gap. That is we placed the IP inside two concentric cylinders. The

outer cylinder consisted of a solid section of aluminum and was 20 cm in diameter, while the inner cylinder was semi-transparent and 16 cm in diameter. Certain plasma properties, such as the axial distribution, depended in the details of the inner boundary windows. The gap between the two cylinders was 1.9 cm while the distance from the edge of the IP electrodes to the inner cylinder was 1.8 cm. In the axial direction the cylinders were 10 cm long, which is twice as large as the 5 cm gap between the IP electrodes. A scaled drawing showing the IP inside the two cylinders is shown in Figure 27. When we mention a "gap" in this report, we are referring to measurements made in the gap between the inner and outer cylinders. A subsection is devoted to each of the following measurements:

1. The plasma axial distribution.
2. The plasma radial distribution.
3. The azimuthal symmetry of the plasma.
4. Spectroscopy on the H plasma.
5. The shot-to-shot reproducibility of the plasma fill.
6. The obtainable mass densities in a POS gap.

6.4.1 The Axial Distribution of Plasma in a POS Gap.

The plasma axial distribution in a POS gap is important since one wants the plasma confined to a discrete region during the conduction phase of the opening switch. Given that the axial distance between the IP electrodes was 5 cm, it would be desirable if the plasma was restricted to a similar width in the POS gap for times of interest. To determine this important relationship we used a single beam interferometer configured in a chordal LOS mode. The beam was focused through the IP plasma to obtain spatial resolutions of 1 mm, and positioned so it passed through the center of the gap. Two small slots were cut in the outer cylinder to allow the beam to pass. With this arrangement, the plasma could be probed from the axial center of the pinch ($z=0$) outward in one direction. The boundary configuration was then inverted axially so z values in the other direction could also be measured for the case of a screened inner boundary. An illustration that shows the positioning of the laser beam and the IP is shown in Figure 28. Four to five shots were taken at each axial position and then averaged. By moving the beam to various axial positions, a relative axial profile could be obtained. Figure 29 shows the results obtained from the set up in Figure 28. These measurements were performed with hydrogen discharges where the

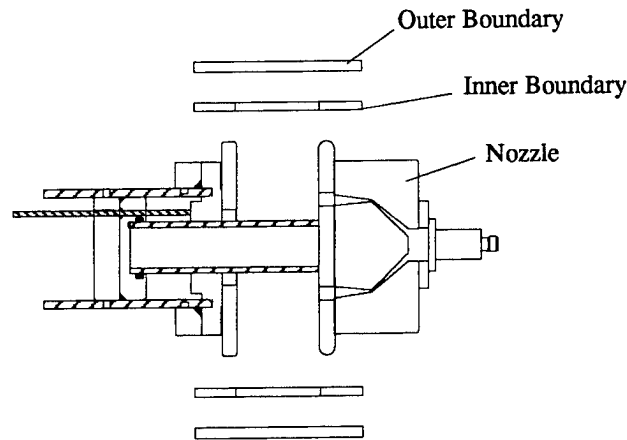


Figure 27. The IP mounted inside two concentric aluminum cylinders. The outer boundary was solid while the inner boundary had four large windows separated by 1/4" bars. Each cylinder was twice as long as the IP electrode separation (10 cm) and the inner and outer gaps were 1.8 and 1.9 cm, respectively.

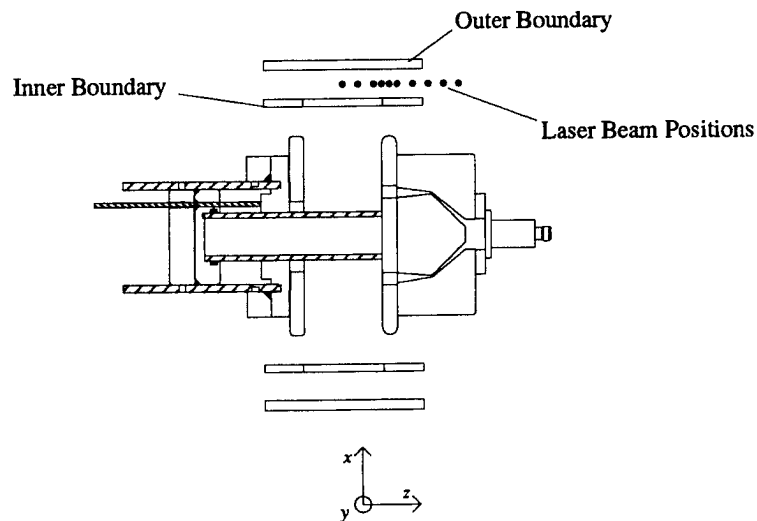


Figure 28. The laser beam positions that were used to measure the plasma axial distribution. Thin slots were cut in the outer boundary to allow the laser to probe the plasma chordally.

inner boundary had 4 large windows that produced a 95% transparent electrode. This data showed that the plasma expanded axially at velocities of 5-8 cm/ μ s, which was comparable to the ejected radial velocity. At a time of 2.4 μ s after the start of current in the IP, the plasma had expanded past the edge of the outer boundary.

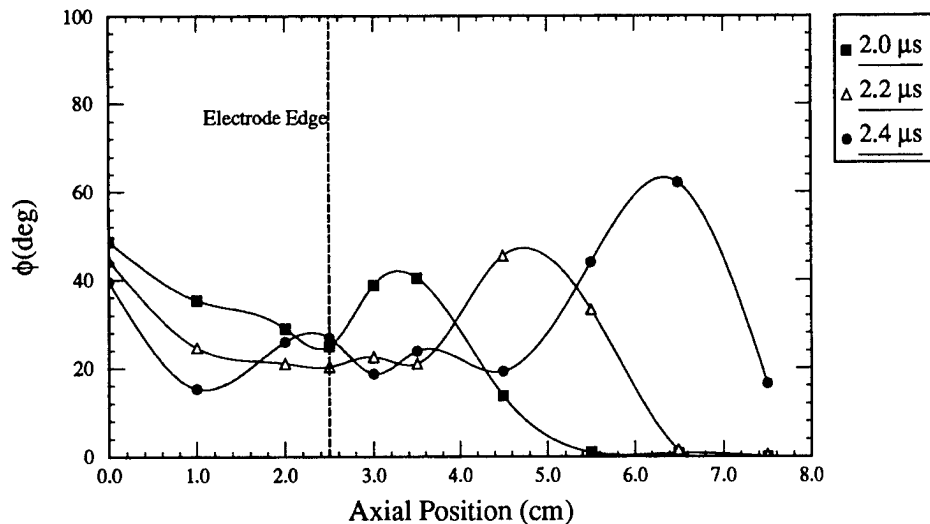


Figure 29. The relative axial distribution of plasma at various times as referenced from the start of current in the IP. This data was obtained by transposing the phase measured at each position as a function of time and indicates an acceleration process in the axial direction. Note that position 0 is the center of the IP and the dotted line indicates the electrode edge.

The data shown in Figure 29 was clearly unacceptable. Furthermore, the magnitude of the axial velocities suggested that this was not simply a thermal spreading process, but rather an acceleration process. To further investigate this we inserted the magnetic loop array in the middle of the gap parallel to the IP axis as shown in Figure 9(b). This probe was oriented to detect an azimuthal magnetic field due to currents flowing in the radial direction. This field/current geometry would give rise to an axial force on the plasma. The integrated signals obtained from the probe array are shown in Figure 30. Each loop was 2 cm apart with axial positions of 1, 3, 5, 7, and 9 cm for loops 1-5 respectively. Based on the results shown in Figure 30, three important observations can be made. The first is that radial currents are flowing at axial positions significantly past the edge of the IP electrode plates at $z=2.5$ cm. (Here $z=0$ is defined in the center between the electrode plates.) The second is that the shape of the radial current flow after the current front has passed the

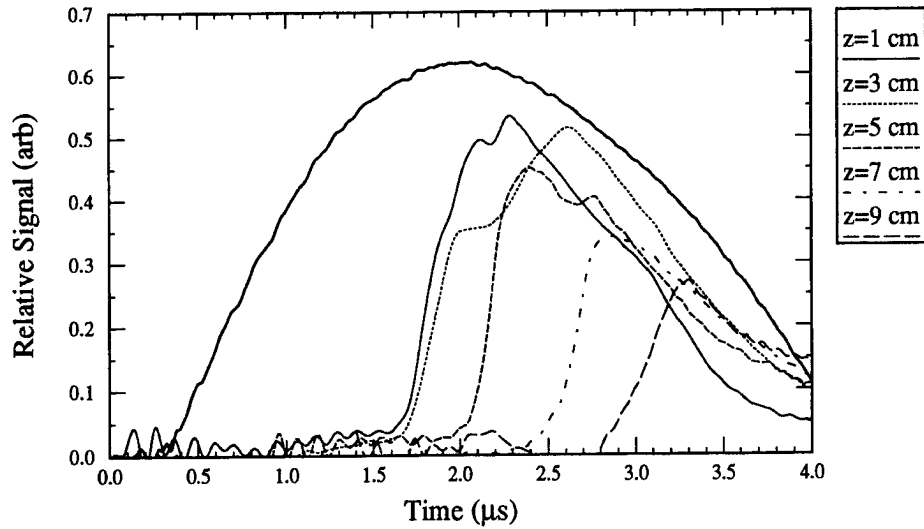


Figure 30. Results from the B-dot loop array arranged axially. Each loop was arbitrarily scaled by the same factor.

loop, is similar to the total current flowing through the IP. The third is the the velocity of the current front outside the electrode plates, ie. that determined from loops 3-5, is roughly the same as the plasma expansion velocity.

These observations support the “spill-over” model shown in Figure 31, that describes the interaction of the current front and the outer boundary. For early times during the IP discharge, ie. before the plasma is ejected, the current flows axially between the IP plates accelerating the plasma radially outward. This phase is shown in part (a) of the figure. When the current front reaches the radial edge of the IP electrodes it is free to expand into the gap since the inner boundary is essentially open (except for the four support bars). Part (b) shows the situation after the current front has hit the solid outer boundary. For times after this, the current may flow from the IP anode through the plasma to the outer boundary and then back through the other edge of the plasma to the IP cathode. In this situation the plasma is accelerated axially via the magnetic field in the POS gap.

To remedy this situation we placed a conducting screen around the inner boundary and used insulators to block the gap between the inner boundary and the IP as shown in Figure 32. With this configuration, the IP operates normally until the current front reaches the screen. At that point the plasma can pass through the screen, but the screen forms a conducting path that terminates the motion of the current front. Therefore, the

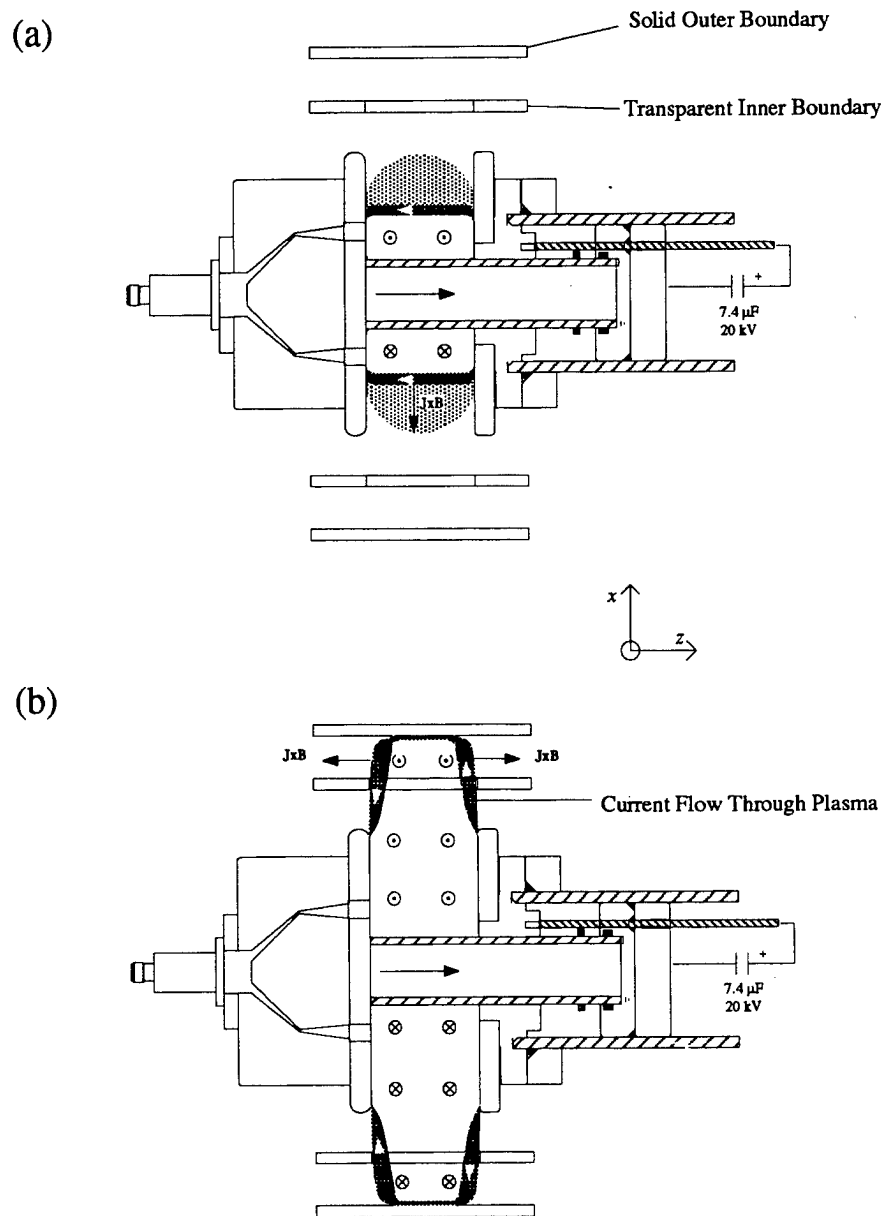


Figure 31. A model to explain the axial acceleration observed with the interferometry and B-dot probes. For times before plasma ejection, part (a), the IP functions normally. After ejection, part (b), the current front can be distorted such that current can flow from one IP electrode through the plasma to the outer boundary and then back through the plasma to the other IP electrode. In this situation the magnetic field will exert pressure axially expanding the plasma in the gap.

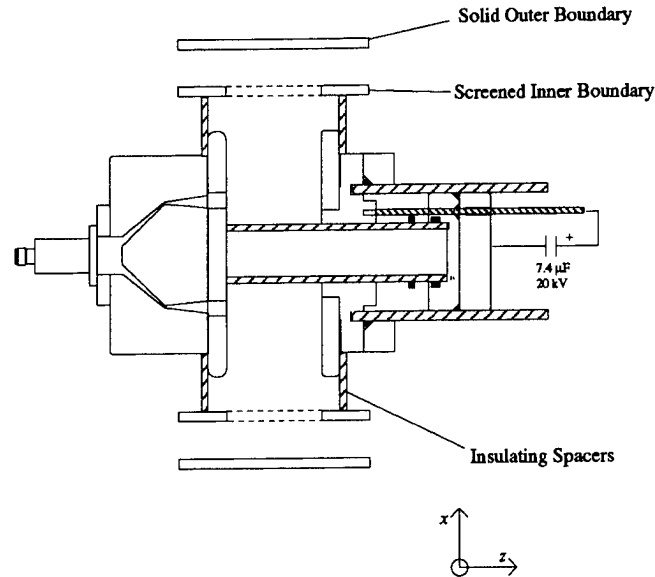


Figure 32. The IP configured with a screen covering the windows on the inner boundary. Also shown are insulating spacers that support the inner boundary and prevent plasma from expanding in the gap between the IP electrodes and the inner boundary.

current front never reaches the POS gap. The insulators that block the gap between the inner boundary and the IP further prevent the current front from expanding axially in that region. We tested the screened configuration with the axially scanning interferometer beam, and magnetic loops. The magnetic loops showed that the radial current flow was removed by the screen, and the bulk of the plasma remained confined to within the dimensions IP electrode plates for times of interest. Only a very small percentage of the plasma expanded outside $z=2.5$. These results (shown in Figure 33) imply a thermal spreading process.

6.4.2 Plasma Radial Distribution.

The plasma radial distribution was measured using the heterodyne interferometer in the axial LOS configuration. The beam was focused through the plasma region yielding a 1 mm spatial resolution. A number of shots were taken at various radial positions between the IP and outer boundary. Figure 34 shows the radial dependence of the electron density for various times after the start of current for H_2 discharges. Qualitatively similar results are obtained with other plasmas, but on a different time scale. At $t=1.6 \mu s$ the plasma has entered the gap and by $3.0 \mu s$ it has reached the outer boundary where one observes a significant buildup on that surface. At later times we observed that the plasma bounced off the outer wall with a

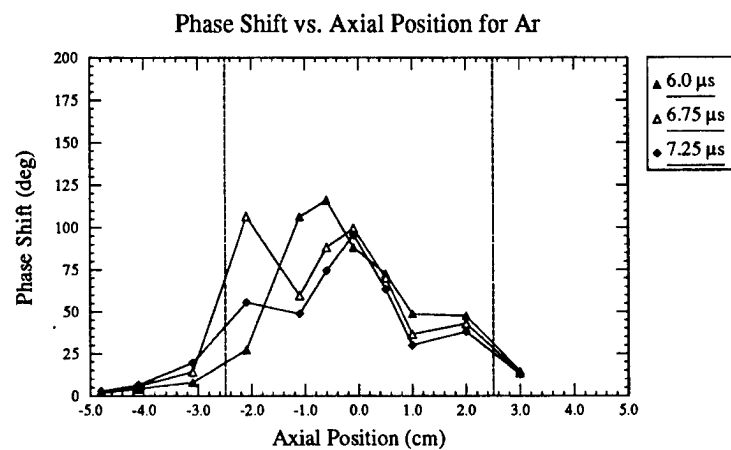
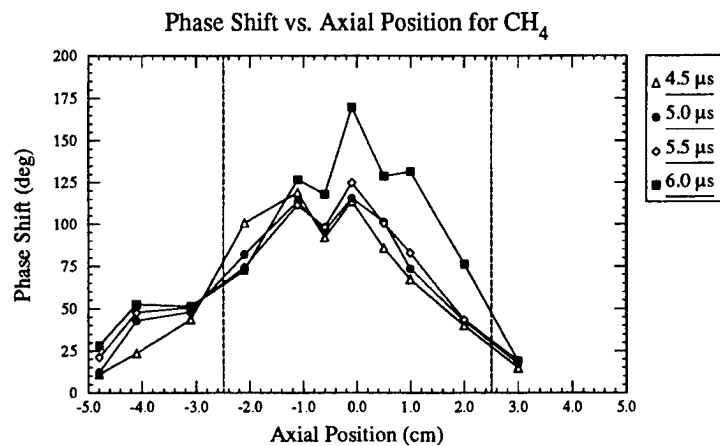
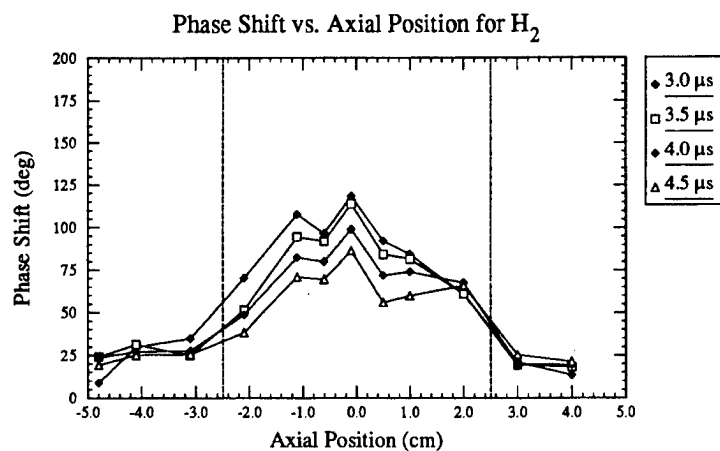


Figure 33. Results from our axial scan measurements. Parts (a),(b), and (c) show results for H_2 , CH_4 , and Ar gases respectively at various times referenced to the start of current in the IP. The dotted vertical lines indicate the edges of the IP electrodes.

significantly reduced velocity. Note that, since the current continues to flow in the IP across the screen, the plasma is prevented from re-entering the IP by the magnetic field inside the IP. As a result we have found that a relatively uniform radial distribution persisted for a few microseconds. Note that on Hawk the outer boundary (anode) was smaller than the boundary that was used for these tests (20 vs. 17 cm). As a result the uniform distribution was reached with shorter delays on Hawk.

6.4.3 Plasma Azimuthal Symmetry.

To investigate the azimuthal symmetry of the plasma, a two channel interferometer was set up using an axial LOS. With this configuration each channel was positioned at the same radius with angular separations that varied from 5 to 51°. A series of shots were performed while monitoring both interferometer channels and varying the angular separation of the two probe beams. Complete agreement between the two interferometer beams would indicate perfect symmetry. We observed that while the agreement between the two interferometer channels was sometimes drastically different for early times, in most cases the agreement improved after the plasma had bounced off the outer conductor. Figure 35 illustrates this point. This plot shows the axially averaged electron density as a function of time for two interferometer beams separated by 30°. Over 100 shots were taken with this type of set up and the data was analyzed statistically. We concluded that the azimuthal variations were $\pm 10\%$ with respect to the average for times after the plasma has bounced off the outer boundary. The larger variation between the two beams observed as the plasma is expanding radially can be explained if the plasma ring is distorted into an elliptical (or some other) shape during the expansion phase. After the bounce off the outer boundary at reduced velocities, the ring is no longer spatially defined and the symmetry improves.

6.4.4 Spectroscopic Measurements on the H Plasma.

Spectroscopic observations were undertaken to help determine the state of the initial plasma that existed during IP/H₂ shots on Hawk. In particular we were interested in the plasma electron temperature, the existence of impurities, and the percentage of neutral hydrogen, if any. To gather the data we used the apparatus shown in Figure 13 with quartz vacuum windows, the McPherson 0.6 m spectrometer, and the OMA detector. We used a boundary configuration that was identical to that on Hawk. With this optical system the spectral range accessible was between 2800-5050 Å. The optical probe was positioned to view the plasma along an axial line of sight at the radial center of the gap between inner and outer boundary in the mocked-up Hawk geometry. The spatial resolution of the optical

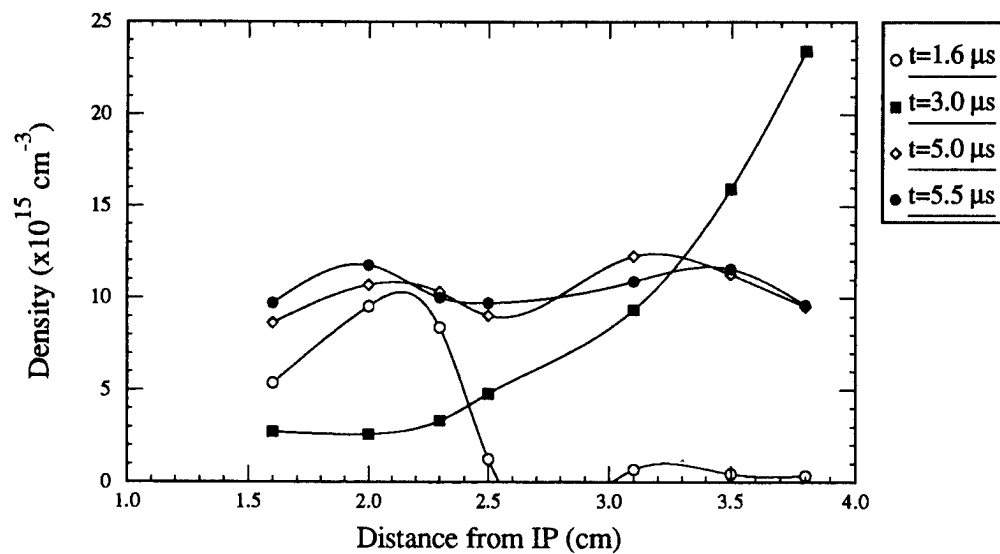


Figure 34. A plot of the plasma electron density as a function of radial position for various times referenced from the start of current flow in the IP. The data was taken between the inner and outer boundaries with a 1 mm laser beam.

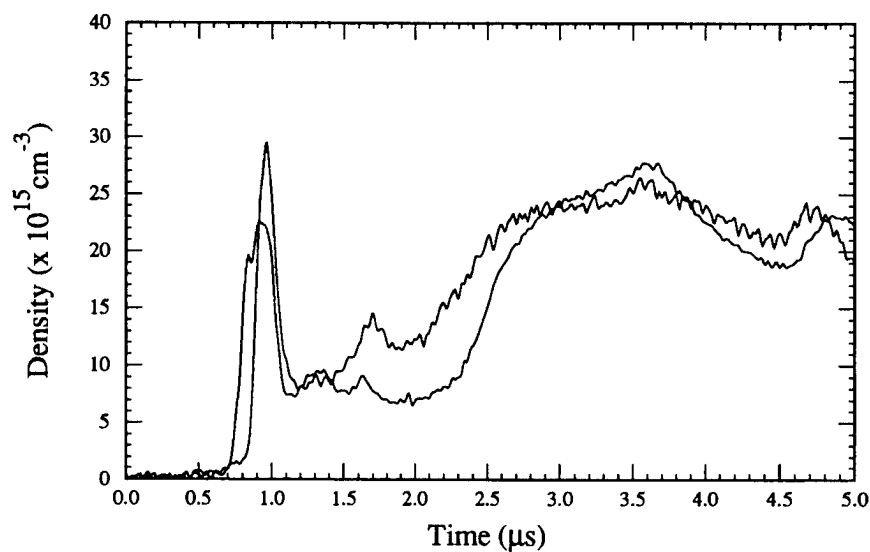


Figure 35. Results from two channel interferometry where the beams are separated by 30°.

Table 2. Summary of the identified impurity lines during an optical survey with the "dirty" IP source operated with H₂ gas.

Species	# Lines	Center Wavelengths(Å)
O I	2	2972,3947
O II	11	3134,3390,3470,3711,3912,3973 4190,4415,4417,4649,4962
O III	4	2984,3047,3265,3754
C II	3	2746,2837,4267
Al I	4	3082,3092,3944,3961
Al II	2	3587,3655

system was 2 mm. These experiments were performed after the Hawk experiments at NRL in early 1998.

Immediately after the Hawk experiments, the IP was visibly dirty with discoloration, as well as chunks of aluminum, on the quartz insulator and electrode surfaces. This debris had accumulated during the course of about 50 POS shots with the generator. We wanted to complete a survey of the optical emission to determine if the debris was being incorporated into the plasma. We used a 3 μ s gate that encompassed the "bounced" plasma and the initial part of the restrike plasma. This was a qualitative experiment as we had no intentions, or means readily available, of absolutely calibrating our optical system to determine ion densities. However, a complete survey in the optical range available to us did show the presence of 26 impurity lines that could be identified. Most abundant of these were O II lines (11). Table 2 above lists the species and number of lines that were identified during this survey. After the survey was complete, the IP was cleaned using acetone and abrasives, and the survey was repeated. With the cleaned IP none of the impurity lines listed in the table were observed. The spectrum was essentially impurity free with only the H I series observable.

Following the survey we continued to make measurements with the hope of determining the plasma electron temperature and the concentration of neutral H in the plasma. Knowledge of the electron temperature would also allow us to calculate ionization rates of impurities that may be desorbed from electrode surfaces. The motivation behind this was to determine if the electron inventory accurately measured the mass of the material in the POS gap during the experiments on Hawk. If a significant amount of material was in the form of neutral atoms or molecules, then interferometry could not be relied upon to measure the injected mass. The only lines available to us, without seeding, were due to the H I spectrum.

In particular we measured the H_α (6563 Å) and H_β (4861 Å) line profiles using the same optical system with the McPherson modified so we could observe longer wavelengths. The OMA detector was used and our gate times were set to coincide with the initial POS plasma that produced the most interesting results on Hawk ($\sim 3.5 \mu\text{s}$ after the start of IP current). Specifically, with reference from the start of current flow in the IP, the gates began around $t = 2.75 \mu\text{s}$ and lasted for 1.0 to 1.5 μs . We also operated a single beam interferometer along the same line of sight (axial) and positioned the interferometer to the same radial position as the optical probe, but at a different azimuth. We investigated three radial positions, one near the inner conductor ($r = 6.7 \text{ cm}$), one near the outer conductor ($r = 8.3 \text{ cm}$), and one in the center of the gap at $r = 7.5 \text{ cm}$. A number of shots were taken with the spectrometer centered on H_α and H_β for each radial position. On each shot we determined the full width at half maximum (fwhm) for each line via fitting of the data to a Lorentz function, the strength of the line as determined by the area of under the line (minus the continuum), and the average value of the electron density during the gate. The relative calibration for H_α/H_β was 3.24, that is to get the proper relative ratio of H_α/H_β we need to multiply the raw data by 3.24. These results were sent to Dr. Y. Maron of Plasma Analyses for interpretation via a time dependent collisional radiative modeling.

There were a number of interesting results from Dr. Maron's analysis, but at this stage we must point out a significant limitation of the measurement. We observed the plasma via an axial line of sight, as a result our optical probe collected light from the plasma edges as well as the center. Further, we viewed emission from H I, which is likely to be more abundant at the edges where we would expect lower electron temperatures. Therefore, our results may emphasize the edge plasma relative to the bulk.

One result of the measurement concerned the width of the H_α line; which we observed to be significantly wider near the outer wall ($r=8.3 \text{ cm}$) compared to other regions in the gap. The difference in widths was significant (2.4 Å vs. 1.7 Å) and can only be explained if opacity had broadened H_α near the wall. That would imply a higher concentration of neutral H in that region, which is a reasonable result from an intuitive standpoint. The most reasonable explanation for opacity of H_α near the wall is that the excited state ($n=2$) is populated via re-combination with slightly higher electron densities than in the center of the gap. The calculations showed that this is possible with only a modest increase in the density at the electron temperature of 0.7 eV. Based on our density measurement the H_β emission should be Stark broadened to about 4.2 Å. We did not observe this, in fact we observed a much narrower line that would imply an electron density of only $0.5 \times 10^{15} \text{ cm}^{-3}$. It is possible that this discrepancy is due to the limitation discussed above where our light

collection system emphasized the edge plasma.

The most critical analysis revolved around the determination of the electron temperature (T_e) and the number density of neutral hydrogen (n_H). The later quantity is of particular importance because if n_H was significant, then interferometry cannot be relied upon to measure the plasma mass. To get the electron temperature, time dependent collisional-radiative modeling was performed while keeping the electron density (n_e) equal to the proton density (n_p) at $3.0 \times 10^{15} \text{ cm}^{-3}$ and varying n_H and T_e as parameters. Possible solutions would be cases where the model predicted that n_e stayed relatively constant for $1 \mu\text{s}$, and the line ratio of H_α/H_β is 8. Both of these constraints are results of experimental measurements. The only electron temperature that produced result within these limitations was $T_e = 0.7 \text{ eV}$. The modeling showed that n_e decreased by only 4% during $1 \mu\text{s}$ and the H_α/H_β ratio was within the experimental error. At higher temperatures, such as 1 eV , the density stayed constant but the H_α/H_β ratio was only 5. At lower temperatures, such as 0.5 eV , the density dropped by 20% over the $1 \mu\text{s}$ due to re-combination, which is also not in accordance with our observations. The analysis also predicted the absolute populations of the excited states of hydrogen which are: $n_2 = 3.9 \times 10^{11}$, $n_3 = 3.9 \times 10^{11}$, and $n_4 = 2.6 \times 10^{11}$, for an electron density of $3 \times 10^{15} \text{ cm}^{-3}$.

Given these relatively low electron temperatures, it is impossible to determine the density of neutral hydrogen (n_H) because the excited states of H are determined by re-combination and **not** by excitations of neutral hydrogen. The quantity of neutral hydrogen will depend on the time history prior to our observations. If large quantities of neutral H or molecular hydrogen (H_2) were injected into the gap, then due to the low T_e , most of them would remain as neutrals on a $1 \mu\text{s}$ time scale. If the converse were true, that little or no neutral material was injected into the gap, then a significant density of neutral material would not be produced as evidenced by the time history of the electron density that stays relatively constant.

Another effect of the low T_e is that desorbed impurities may not be sufficiently excited to observe optical emission. Here we must be careful to distinguish between desorbed material and impurities incorporated into the IP plasma. By the former we refer to molecules that are knocked off material surfaces (such as the outer boundary) by the plasma. Clearly we can observe the latter (IP plasma impurities) as evidenced by the results in Table 2 obtained using a "dirty" IP, but desorbed matter in such a low temperature plasma may be "dark" and remain neutral until the electrons are heated. Such heating would certainly take place when the generator current starts in a POS.

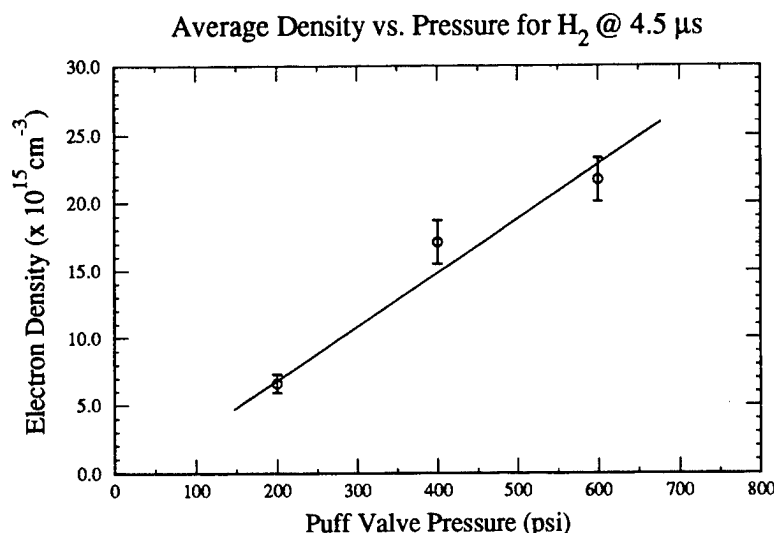


Figure 36. A plot showing the relationship between the average electron density in the gap and the pressure behind the puff valve. Pressures from 200 to 600 psig were investigated. Note that the POS gap configuration, as well as the puff valve delay, was significantly different from later experiments on Hawk.

6.4.5 Plasma Reproducibility.

An important consideration is the consistency with which the IP can fill a POS gap with plasma, or the variation from shot to shot. To investigate this issue we performed a series 10 shot runs while monitoring the electron density with an axial LOS interferometer. The interferometer beam was positioned in the radial center of the gap. A series of 10 shot runs were taken using H_2 and Ar gases under various conditions. For times after the plasma distribution has become uniform ($4\text{--}5 \mu\text{s}$ for H, $5\text{--}6 \mu\text{s}$ for Ar) an average density was obtained for the 10 shots. Typically, average deviations were $\pm 10\%$ for both gases. As an example we found that at $4.5 \mu\text{s}$ the electron density in the H plasma was $14.4 \pm 1.3 \times 10^{15} \text{ cm}^{-3}$ and at $5.0 \mu\text{s}$ the electron density in the Ar plasma was $8.1 \pm 0.9 \times 10^{15} \text{ cm}^{-3}$.

6.4.6 Mass Density Control.

The IP is a versatile device in that the mass density can be controlled at two levels. The rough, or coarse, control is the type of gas the one uses. This will change the mass density in large steps by changing the species of ions in the plasma. At the same time a more exact control is available. By varying the pressure behind the puff valve, which in turn varies the size of the gas puff, a certain amount of density control is realized. Figure 36 illustrates this

Table 3. The estimated average mass densities obtainable using the IP and various gases. The units are $\times 10^{17} m_p/\text{cm}^2$.

Pressure	H ₂	CH ₄	Ne	Ar
200	0.32	2.7		6.8
400	0.86	3.5	7.9	9.8
600	1.1	4.2		

control. In this case the pressure of the H₂ gas puff was varied from 200 to 600 psig while keeping the puff valve delay constant, and a corresponding increase in the electron density was observed. Similar relationships have been observed with Ar and CH₄ plasmas.

A wide range of mass densities can be reached using the IP with various gases and puff valve pressures. We have experimented with H₂, CH₄, Ne, and Ar. All these gases, with the exception of Ne, operate reasonably consistent with the ability to reproduce plasma densities to within $\pm 10\%$. We have not been able to discover a regime where Ne discharges become as consistent. This may be due to its relatively high first ionization potential at 24 eV. Based on the data that we have, we can estimate the mass densities that each type of gas can produce. It will be assumed that the average ionization states are Ar⁺² and Ne⁺². It is further assumed that the methane molecules are completely broken down so that 3.8 electrons are produced for each CH₄ in accordance with Table 1. Table 3 shows the line integrated mass densities, in units of $\times 10^{17} m_p/\text{cm}^2$, that can be achieved based on our measurements of the electron densities for various gases and puff valve pressures. The results indicate that a variation of nearly two orders of magnitude has been observed, with a potential of even higher mass densities using heavier gases such as Xe or Kr.

Section 7

Results of POS Experiments on Hawk

In this section we will summarize the POS experiments using the IP as a plasma source. These experiments took place on the Hawk generator at the Naval Research Lab. The Hawk machine [8] (720 kA, $1.3 \mu\text{s}$ quarter period) has been used in the past for numerous POS experiments with various plasma sources such as flashboards,[9] cable guns,[10] and coaxial gas plasma guns.[11] Figure 1 shows a scaled drawing of the IP source mounted inside the generator.

7.1 Hardware and Diagnostics.

Certain hardware modifications were needed for the source and generator before the experiments could begin. The outer diameter of the IP was reduced from 12.7 to 9.5 cm and we manufactured a new aluminum center conductor (cathode) for Hawk with an outer diameter of 12.7 cm. Taking into account the wall thickness of the center conductor (1 cm), there was a 6 mm gap between the outer edge of the IP and the inner edge of the cathode. This space was needed to electrically isolate the IP from the generator and feed gas lines across the IP electrodes inside the cathode. A series of 18 equally spaced apertures in the center conductor allowed the plasma to enter the inter-electrode region. Each of these windows was 5 cm long to match the spacing between the IP electrodes. The bars between each aperture were 0.32 cm thick rendering the cathode 86% transparent. For the outer conductor (anode) we used an existing electrode with a 17 cm inner diameter. The anode was solid in the POS gap region to provide a surface for the plasma to bounce off of and fill the gap. The load was a short circuit located 33 cm downstream from the center of the switch. Both electrodes were designed so they could be inverted axially which allowed us to conduct experiments with cable guns, where the plasma sources are arranged around the outside, using the same electrode geometry.

Machine diagnostics included generator voltage and current probes, and three sets of anode current probes located 6, 22, and 32 cm downstream from the center of the switch. The anode current probes, shown in Figure 1, are shielded magnetic pick-up loops. A Rogowski coil located near the capacitor bank, was used to monitor the IP current. The plasma

electron density was measured using an axial line-of-sight, 8 channel, He-Ne heterodyne interferometer.[5] Each beam sampled the plasma at a different radial position over the range from $r = 6.5$ cm to $r = 8.5$ cm with equally spaced intervals. As a result the temporal evolution of the radial density profile, as well as the total electron inventory, could be measured on each shot.

7.2 POS Shots Using the IP.

Experiments were performed using various gases (H_2 , Ne, Ar, Air) as well as cable guns for comparison. There were a total of 71 recorded POS shots with the IP. A summary of each shot indicating the puff valve pressure, puff valve delay, IP delay time, conduction time T_c , conducted current I_c , peak switch voltage V_{POS} , and initial electron density are shown in Table 4. The IP delay time is the time interval between the start of current flow in the IP and the start of the generator current, the conduction time was defined as the time interval from the start of the generator current to the time when the load current reaches 10% of its peak value. In the table we try to indicate the initial electron density. For cases where a \sim symbol appears in front of a value the density profile was relatively uniform as shown in Figure 34, and we indicate the average density. In cases where there was a positive or negative density gradient the $>$ and $<$ symbols denote them respectively, and the density range is given. In many cases only one channel of interferometry was available (most of the Ar shots), this is indicated by an asterisk (*) and we give the electron density near the radial center of the gap.

It is clearly evident that POS shots using H_2 gas exhibited significantly higher values of load dI/dt , but only for those cases where the IP delay time was $\sim 3.5 \mu s$. This delay time corresponds to the conditions where the radial distribution was uniform and static on $1 \mu s$ time scales. When compared to typical cable gun shots, the IP/ H_2 POS was very impressive. These features of the IP/ H_2 POS are best illustrated in Figures 37 and 38. Figure 37 shows typical load currents for a cable gun shot, an IP/Ar shot, and an IP/ H_2 shot with a long delay time. In each case the conduction times are very close, and we see that the IP/ H_2 shot transfers current to the load much faster than the other two cases. Figure 38 illustrates the dependence of the POS voltage on the plasma initial conditions. This plot shows the voltage at the center of the switch as a function of the conduction time. There are three types of data points corresponding to three different types of initial radial distributions that were shown in Figure 34. A curve is also shown that reflect the data obtained using cable guns. In this plot we can clearly see that only for the uniform initial plasma distribution do we get voltages that are significantly larger than any other type of shot.

Table 4. A log of all the IP shots on Hawk.

Inverse Pinch/Hawk Data								
Shot #	Gas	Pres. (psig)	Puff Delay (μ s)	IP Delay (μ s)	T_c (ns)	I_c (kA)	V_{POS} (kV)	$n_e(t=0)$ ($\times 10^{15} \text{ cm}^{-3}$)
2649	H ₂	800	400	1.9	899	610	99	> 3.5-5.0
2650	H ₂	800	400	2.1	920	620	134	> 2.8-5.8
2652	H ₂	800	400	1.9	932	600	91	> 4.3-6.0
2655	H ₂	800	400	2.1	950	605	169	> 2.5-4.7
2656	H ₂	800	400	1.0	800	575		< 2.0-1.0
2657	H ₂	800	400	1.4	880	610	74	< 7.0-2.0
2658	H ₂	400	400	1.3	885	585	78	< 3.3-0.5
2659	H ₂	800	400	1.5	1015	615	60	> 0.0-7.0
2665	H ₂	600	350	2.2	699	490	174	> 1.0-9.3
2666	H ₂	600	350	2.2	678	490	177	> 1.5-13.0
2667	H ₂	600	350	2.2	678	490	231	> 1.4-10.3
2668	H ₂	600	350	3.7	852	580	321	~ 3.7
2669	H ₂	600	350	3.6	858	575	301	~ 4.7
2671	H ₂	400	350	3.6	814	560	281	~ 3.1
2672	H ₂	200	350	3.6	608	450	182	~ 1.8
2673	H ₂	100	350	3.4	463	360	117	~ 0.74
2674	H ₂	800	350	3.6	932	595	286	~ 5.5
2690	Ar	100	700	4.1	743	515	126	1.1*
2691	Ar	100	700	4.6	844	610	85	?
2692	Ar	100	700	3.1	710	570	119	2.2*
2693	Ar	100	700		833	575	111	2.7*
2694	Ar	100	700	9.7	969	600	152	2.8*
2695	Ar	100	700	10.7	950	605	111	?
2696	Ar	100	700	10.7	704	575	157	1.3*
2697	Ar	100	700	11.6	767	590	99	1.5*
2700	Ar	100	700	10.7	887	585	121	0.64*
2701	Ar	100	700	13?	806	550	80	0.67*
2702	Ar	100	700	10.8	1012	625	115	1.7*
2704	Ar	100	700	5.9	683	475	79	1.3*
2705	Ar	200	700	10.8	1214	681	94	?
2706	Ar	200	700	11?	1205	666	106	3.0*
2707	Ar	200	700	10.7	1190	665	112	3.1*
2708	Ar	50	700	10.7	544	415	80	0*
2709	Ar	50	700	6?	637	475	94	2.4*
2710	Ar	75	700	10.7	832	550	146	1.4*
2713	Ar	75	700	11?	779	555	98	0.34*
2714	Ar	75	700	10.5	690	500	111	0.96*

Table 4. A log of all the IP shots on Hawk (Continued).

Inverse Pinch/Hawk Data (continued)								
Shot #	Gas	Pres. (psig)	Puff Delay (μ s)	IP Delay (μ s)	T_c (ns)	I_c (kA)	V_{POS} (kV)	$n_e(t=0)$ ($\times 10^{15} \text{ cm}^{-3}$)
2715	Ar	150	700	10.5	1090	630	90	1.8*
2716	Ar	150	700	10.5	1043	625	108	1.8*
2717	Ar	150	700	10.5	1050	625	87	1.7*
2718	Ar	100	700	11?	1034	620	115	> 1.1-3.1
2722	Air	300	500	9.5	1184	660	93	?
2723	Air	300	500	9.4	639	470	76	> 0-2.3
2724	Air	300	500	9.4	768	530	117	\sim 1.7
2725	Air	300	500	3.8	752	530	166	> 0-3.3
2726	Air	300	400	4.5	1015	610	129	\sim 1.4
2727	Air	300	400	6.0	641	450	114	> 0-2.0
2728	Air	300	400	7.1	636	450	103	> 0.5-2.1
2729	Air	300	400	8.1	660	480	111	> 1.6-3.3
2730	Air	300	400	8.9	684	465	124	\sim 1.4
2731	Air	300	400	10.4	819	535	103	> 0-1.6
2732	Air	300	400	11.3	520	400	81	?
2733	Air	300	400	9.0	655	495	89	?
2734	Air	300	400	9.4	520	400	108	\sim 0.7
2735	Air	300	500	9.0	631	460	107	> 0-1.2
2736	Air	400	400	9.0	656	470	93	\sim 1.0
2739	Ne	250	450	4.7	1009	600	75	0.6-2.5
2740	Ne	250	450	4.2	814	535	87	1.5-3.6
2741	Ne	250	450	3.7	695	490	86	> 1.8-3.0
2742	Ne	250	450	4.7	855	575	53	< 3.4-1.6
2743	Ne	250	450	3.7	753	515	89	> 0.6-2.4
2744	Ne	250	450	3.3	686	480	102	> 0.8-2.1
2745	Ne	250	450	4.1	850	570	106	\sim 3.2
2746	Ne	250	450	3.5?	779	540	83	\sim 1.8
2747	Ne	300	450	3.8	761	515	102	> 1.6-3.7
2748	Ne	400	450	3.8	660	470	157	> 0.6-1.2
2749	Ne	500	450	3.8	676	480	115	> 0.3-1.3
2750	Ne	600	450	3.8	739	490	151	> 0.1-1.4
2751	Ne	800	450	3.8	802	505	119	> 0.4-1.5
2752	Ne	1000	450	3.7	708	485	143	> 0.5-1.4
2753	H ₂	600	350	3.6	925	600	280	\sim 3.6
2754	H ₂	600	375	3.6	953	605	377	\sim 5.1
2756	H ₂	600	400	3.6	1028	625	217	\sim 5.2
2757	H ₂	600	325	3.5	643	465	196	\sim 1.8
2758	H ₂	600	375	3.7	985	610	264	\sim 4.7

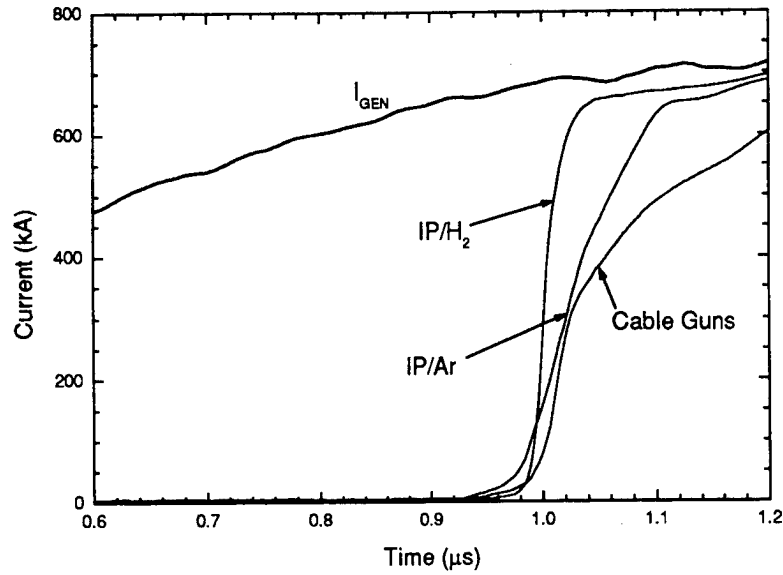


Figure 37. Load current traces that were obtained during the POS experiments with the IP on Hawk. A representative generator current waveform and load current waveform using the cable gun source is also shown.

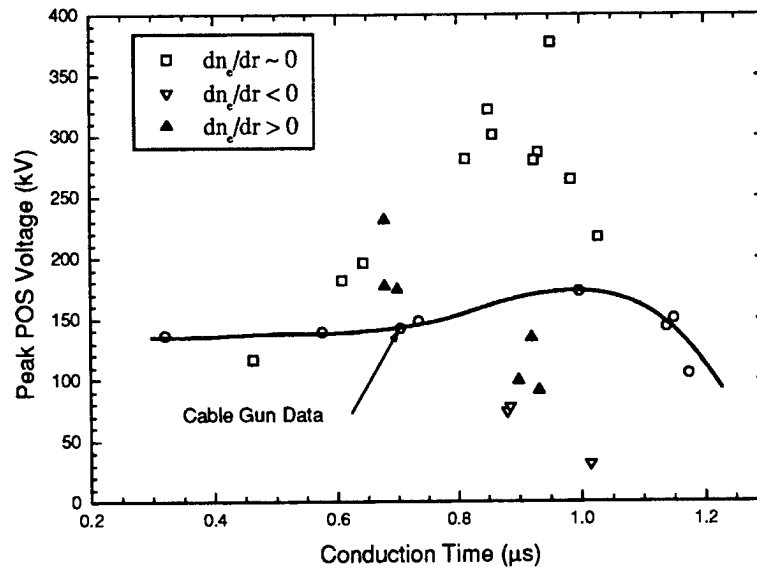


Figure 38. The peak recorded switch voltage vs. the conduction time for IP shots on Hawk using H₂ gas. The data is separated according to the initial density gradient in the plasma fill. A curve representing to the cable gun data (open circles) is also shown.

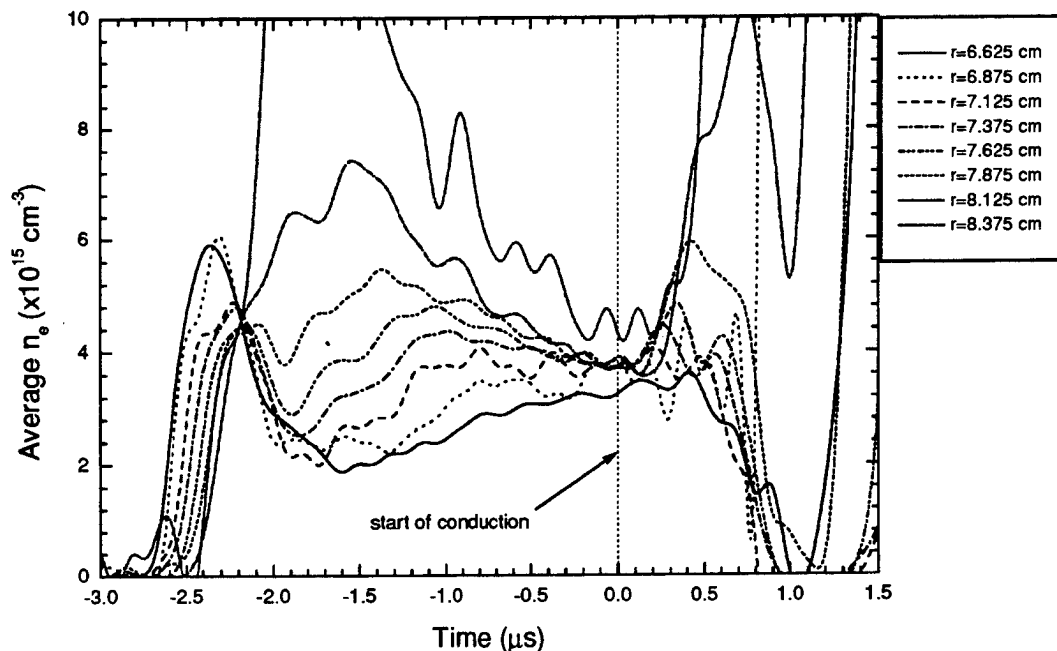


Figure 39. A plot of the average electron density vs. time obtained during an IP shot on Hawk with H_2 gas. In this case we can see that at the start of conduction ($t = 0$), the density is very nearly uniform.

7.2.1 Density Evolution: Conduction Phase for IP/ H_2 Shots.

The 8 channel interferometry gave us the ability to observe the density evolution in the POS gap under the assumption of azimuthal symmetry. The 8 detectors essentially span the entire radial gap with the exception of approximately 1 mm from each respective surface. The average electron density was obtained from the interferometer signals by using the nominal plasma length of 5 cm with a resolution limit of about $\pm 3^\circ$ or $\pm 5.8 \times 10^{14} \text{ cm}^{-3}$. Figure 39 shows the average electron density as recorded on all eight channels for shot #2754 that used H_2 gas with a $3.6 \mu\text{s}$ delay. Channel 1 was centered at the smallest radial position near the cathode ($r = 6.625 \text{ cm}$), channel 8 centered near the anode at $r = 8.375 \text{ cm}$, and the center-to-center spacing for each channel was 2.5 mm. In this figure we have defined time $t = 0$ at the start of the generator current. There are a number of interesting features in this data that will be elaborated on in this section. Before the generator starts, at about $-2.6 \mu\text{s}$, we observe sharp peaks in the density for each successive channel starting with channel 1

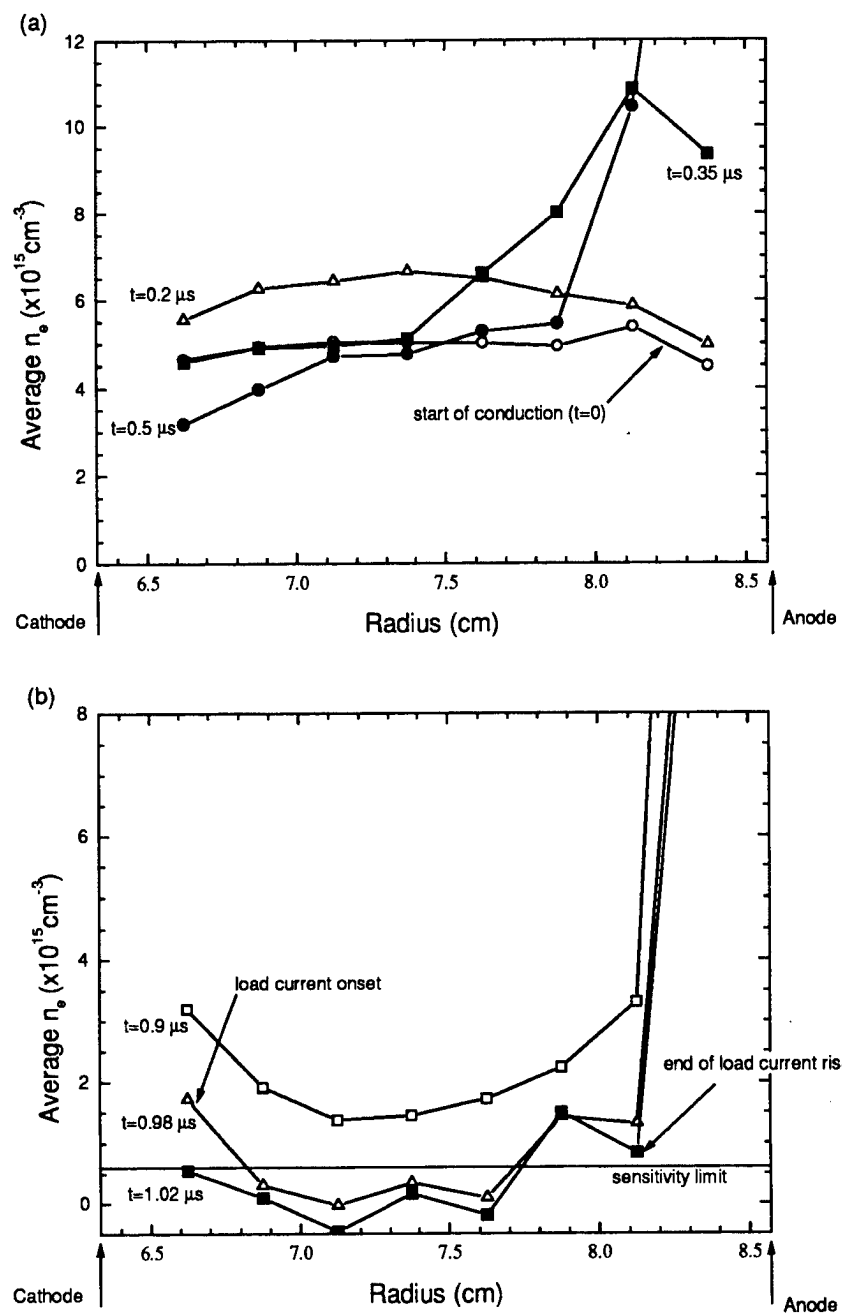


Figure 40. The average electron density vs. radius obtained during an IP shot on Hawk with H_2 gas. Part (a) shows early times where an increase in the electron density at all radial locations is observed. Part (b) shows the data later in the conduction phase and during opening where a large radial region shows density levels below the sensitivity limit of the interferometer.

and moving radially outward. This signature is the plasma ring expanding radially. When channel 8 (near the anode) rises off the scale of the figure ($-1.6 \mu\text{s}$), it indicates the time when most of the plasma has stagnated against the anode. Finally near $t = 0$ the distribution evens out and becomes uniform as we have discussed in a previous section. Very soon after the generator current begins ($\sim 150 \text{ ns}$) the density is observed to increase on the channels closest to the cathode, and very soon after a density increase is observed on the channels nearer the anode. The increase nearer the anode is larger in magnitude. Figure 40(a) shows the average electron density vs. the radial position at selected times early in the conduction phase where one can see that the increase was first observed near the cathode and later at the anode, increasing in magnitude. We must keep in mind that a pure, fully ionized hydrogen plasma cannot generate additional electrons. It is clear from Figure 40(a), that the electron inventory had increased forcing us to conclude that ionization of contaminants or neutral hydrogen had occurred. Another way to look at the data is to calculate the electron inventory as a function of time. An approximation to the total number of electrons in the POS gap (N_e) was calculated from the measured phase shift at various radii ($\phi(r)$) via the following equation:

$$N_e = 2\pi C \int_{r_K}^{r_A} \phi(r) r dr \approx 2\pi C \Delta r \sum_{i=1}^{i=8} r_i \phi_i, \quad (7)$$

where C is a constant that converts phase shift to line integrated density, Δr is the spacing between interferometer channels, r_i are the center radii of each channel, and ϕ_i are the measured phase shifts at each channel. This sum was calculated as a function of time and the results are shown in Figure 41 where N_e is in units of $\times 10^{17}$, and the sensitivity limit is shown as a horizontal line. Two calculations were performed, one that included all 8 channels and the other that used only the interior six channels. The later calculation emphasizes the removal of plasma during opening. This plot makes it quite clear that there is a substantial increase in the total number of electrons ($\sim 40\%$) during the conduction phase.

7.2.2 Density Evolution: Opening Phase for IP/H₂ Shots.

During the opening phase we observed a dramatic decrease in the plasma density such that the values were below the sensitivity limit over a span encompassing the interior 4 to 6 interferometer channels (1-1.5 cm). Such behavior has never been observed on Hawk with other sources.[12] Figures 40(b) and 41 both display this feature which was common to all IP/H₂ shots with long delays. Not only are the large “gaps” unique, but the density remains low throughout the entire opening phase for as long as $1 \mu\text{s}$ after opening begins. The later

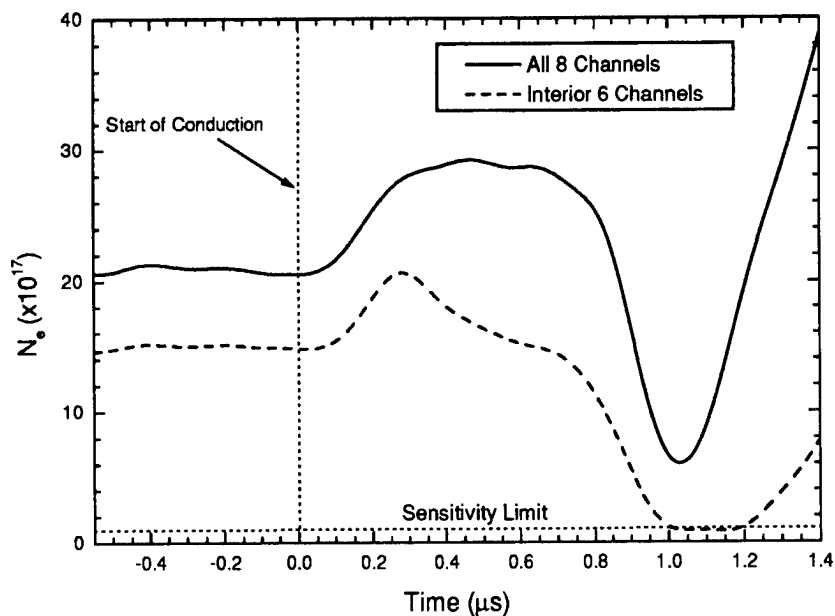


Figure 41. The total number of electrons measured by the 8-channel interferometer vs. time during an IP shot on Hawk using H_2 gas. The dashed line shows the number of electrons calculated from the interior six channels.

feature is best displayed in Figure 41 that contains a curve of N_e as a function of time for the interior 6 channels.

7.2.3 Density Evolution: IP/Ar Shots.

Unfortunately, only one channel of interferometry was available for most of the IP/Ar series. This was due to dirty vacuum windows that forced us to reduce to number of channels so the signal to noise ratio of the laser detector could be increased. There was one shot (#2718) where all 8 channels were operating. The density evolution is similar to the IP/ H_2 shots with one notable difference; the initial distribution is not very uniform in comparison to the hydrogen plasma case. However, we saw a similar increase in the electron inventory followed by a sharp decrease in the density on most of the 8 channels near opening. It should be pointed out that for the same electron densities in a hydrogen and argon plasma, the mass density is approximately a factor of 20 greater for argon. The exact number depends on the ionization state of argon, but the point is that for any reasonable ionization state the interferometer is much less sensitive to the mass density for Ar plasmas.

7.2.4 Scaling of POS Current.

The relationship between the conducted POS current and the properties of the injected plasma has been the subject of many publications.[13, 14, 15, 16] It is generally agreed that the conducted current of switches where the IT product is in the range of 1 MA- μ s will obey MHD scaling. The MHD scaling theory is conceptually simple and is adequately described by a snowplow model where an ideal snowplow pushes the switch plasma axially via $\mathbf{J} \times \mathbf{B}$ forces. The end of the conduction phase is defined when the snowplow reaches the end of the switch length, this is also equivalent to the plasma center of mass being displaced one half the switch length. According to MHD scaling, the relationship between the conducted current and the plasma properties is the following:

$$\int_{t=0}^{t=T_c} I_g^2(t) dt^2 = \frac{100\pi r^2 l^2 M n_e}{Z}, \quad (8)$$

where $I_g(t)$ is the generator current, r the cathode radius, l the axial switch length, M the ion mass, Z the average ion charge, n_e the electron density, and T_c the conduction time. The conducted current I_c is simply equal to $I_g(T_c)$. This relationship implies that the conduction is governed by the plasma mass density (Mn_e/Z). For the case of hydrogen we have $M/Z = 1$, and we would require a higher electron density to conduct the same IT product than a heavier mass plasma such as Ar, where M/Z might be ~ 20 . Our experiments with the inverse pinch gave us the opportunity to check the scaling with different species plasmas. Figure 42 is a plot of the conducted current vs. the electron density that includes data compiled from IP/Ar and IP/H₂ shots, along with several calculations based on the MHD theory for different ratios of M/Z . For the data we only included IP/H₂ shots with a long delay time when the density was approximately uniform. For the Ar data we assume uniformity (only one channel of interferometry data was available) and pick the shots with a long delay time (10-11 μ s). The Ar data fits reasonable well to a curve with $M/Z=20$, implying an average charge state for Ar of +2, which agrees with the ionization state determined from our snowplow calculation (see Table 6-1). However, the H₂ data is not even close to the curve that would correspond to a pure hydrogen plasma, namely $M/Z=1$. In fact, the IP/H₂ data fits MHD theory if we assume $M/Z=6$. One way to explain this under the guise of MHD theory, would be to account for the extra mass as neutral hydrogen that exists before the generator current starts. The neutral mass must be ionized during the conduction phase to contribute to the MHD process. Figure 42 implies that there would have to be 5 times more electrons/protons than what is initially detected at $t = 0$, and we should see an increase in the electron inventory by a factor of 5 during the conduction phase. The fact that we see only a 40% increase in the electron inventory is strong evidence that neutral

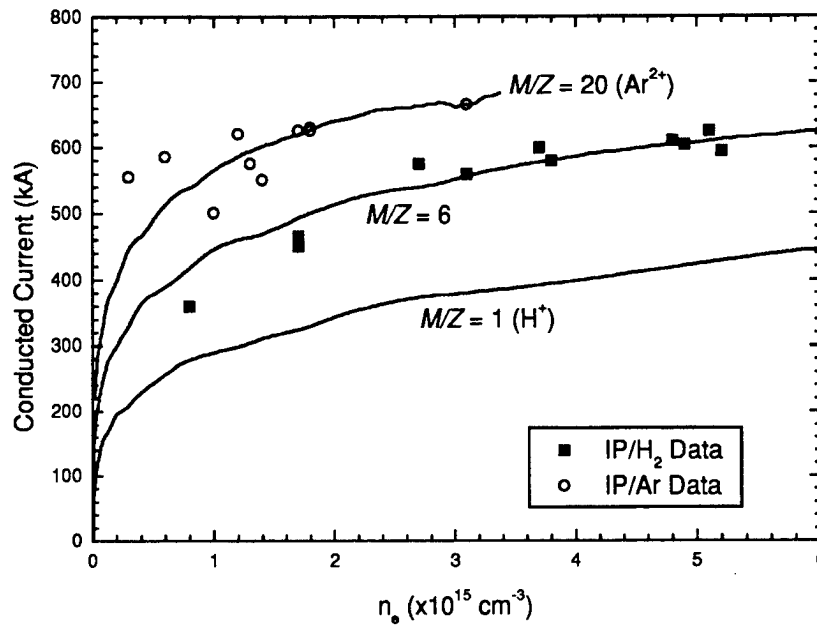


Figure 42. The conducted current vs. the injected electron density for IP shots on Hawk with Ar and H₂ gas. Only the H₂ data with uniform initial density distributions are displayed. Also shown are three curves that were calculated from MHD theory for various M/Z ratios indicating that a $M/Z = 6$ fits the H₂ the best.

hydrogen is not contributing significantly to the increased mass. A more likely scenario is that the plasma desorbs vacuum system impurities, and possibly aluminum, from the electrode surfaces. These impurity atoms may exist as neutral material at $t = 0$, and would even go undetected spectroscopically due to the low electron temperatures ($T_e = 0.7 \text{ eV}$).^[17] If these impurities were ionized during the conduction phase with an average $M/Z=12.5$, then the MHD theory can account for the observed IT product. It seems conceivable that the ionization of Al and common vacuum system adsorbates (CH₄, H₂O, CO) could produce a plasma with a mass to charge ratio of 12.5.

7.2.5 Comments on IP/Air and IP/Ne Shots.

A number of POS shots were tried using the inverse pinch with Air (15) and Ne (14). Using the IP with Air had not been tried before, and there was an uncertainty surrounding the expected performance of the IP from the standpoint of a plasma source. We did have some prior experience using Ne and we knew that the IP did not perform well. Ne discharges

were plagued by inconsistent breakdowns for all combinations of puff valve delays and pressures that were tried in the past. Despite this, we were motivated by the desire to try an intermediate mass plasma. We had shown that methane (CH_4) worked very nicely using the IP, but this gas was unavailable at the time. Using Ne and Air we were never able to reach the level of operation achieved with Ar. An examination of Table 4 shows this to be the case. Because of the POS results, and the uncertainty surrounding the IP performance as a plasma source using these gases, most of this data remains unanalyzed.

Section 8

Conclusions

In summary, we have successfully designed and tested a plasma source with inverse pinch geometry. The source derives its plasma from a gas puff and requires a 20 kV, ~ 125 kA, $1.5 \mu\text{s}$ quarter period pulse for operation. We have demonstrated reasonably consistent ($\pm 10\%$ for most parameters) operation using H_2 , CH_4 , and Ar gas with the IP mounted in a POS-like geometry. We have verified the IP operates like the inverse of a gas puff z-pinch using framing photography, magnetic pick-up loops, and interferometry. Furthermore, we have characterized the fill plasma by measuring its radial and axial distributions and determined appropriate semi-transparent boundary that prevents current flow in the POS gap. Near the conclusion of the program we fielded the source on the Hawk POS at NRL that produced very interesting data. We feel that some discussion of these experiments is warranted.

The results from the POS experiments on Hawk raise a number of interesting questions with regard to POS physics issues and show a great deal of promise for improving POS parameters using a hydrogen plasma. The fact that switch voltages were significantly higher using hydrogen plasma makes it tempting to conclude that a plasma dominated by low mass ions will improve the switch characteristics. While this may be true, it is also a gross simplification because we have found that the state of the initial plasma may play an equally important role. The shorter delay times, when the plasma distribution was changing on $1 \mu\text{s}$ time scales, produced results that were essentially indistinguishable from cable guns. It was only at the longer delays that we saw significant improvement using hydrogen. It should be emphasized that, because the IP source ejects a discrete plasma ring, changes in the delay time redistribute the same quantity of plasma in the gap. While the radial density profiles become uniform for the long delays, other plasma properties, such as the azimuthal symmetry and radial velocity, may also change significantly. It is therefore unclear which of these properties is responsible for the improved performance.

The scaling of the conducted current with the injected plasma mass, in particular the hydrogen data (see Figure 42), raises the issue of secondary plasma formation during the conduction phase. If a pure, fully ionized, hydrogen plasma is assumed to exist prior to the

start of the generator current, then there is not enough mass to account for the observed conduction according to MHD scaling. However, if the plasma is not fully ionized then the mass may be significantly higher. The fact that we observed an increase in the electron inventory by 40% during the conduction phase (Figure 41) indicates that we have ionized either neutral H or H₂ originating from the gas puff, or ionized desorbed material from the electrode surfaces (aluminum). If these additional electrons produced ions with $M/Z=12.5$, then the data would agree with MHD scaling. It is conceivable that an ionized mixture of common vacuum system adsorbates (H₂O, CH₄, CO) and aluminum can account for this additional mass. The overall scenario that plasma formed from adsorbates had contributed to the conduction is not inconsistent with our spectroscopic measurements on the H fill plasma that showed no impurity emission. The analysis of this data indicated that the electron temperature was very low in the fill plasma, which introduces the possibility that desorbed material could exist, but not be sufficiently excited to produce optical emission. Emission would only be observed when the electrons are heated, say by the generator current.

Perhaps the most significant result with regard to improvements in the POS is the observation of large areas where the electron density falls below the sensitivity limit of the interferometer as shown in Figure 40(b). This type of behavior has not been observed with other plasma sources.[12] If this region evolves into a magnetically insulated vacuum gap, then we would expect higher voltages/power coupling into diode loads than is presently achieved in POSs.

The authors would like to acknowledge the help of Ms. Pat Herbert of DSWA for her efforts to get this program funded, and Dr. Ralph Schneider, also with DSWA, for his continuing support. We also appreciate the expert technical help by HY-Tech personnel, specifically Dan Steinberg and Caterina Vidoli. Many of the early design elements of the IP were a direct result of conversations with Dan, and Caterina was an essential member of our team, especially during the experiments at NRL. Dr. Hylton Murphy of Maxwell Technologies assisted us by making useful suggestions in the design of the gas nozzle. Finally, we would like to thank the entire technical staff at NRL for their support during the experiments on Hawk. In particular the authors appreciated the enthusiastic response on the part of Dr. Robert Commisso and Dr. Bruce Weber to the prospect of using the IP on Hawk. Bruce also deserves special mention for his consultation and efforts in analyzing the data.

Appendix

Bibliography

- 1 J. Marshall, I. Henins, R. Dike, and J.L. Tuck, "Status Report of the LASL Controlled Thermonuclear Research Program for 12 Month Period Ending October 31, 1966," (UNCLASSIFIED) Rep. # **LA-3628 MS**, p. 69 (1966).(UNCLASSIFIED)
- 2 J.H. Lee, S.H. Choi, and K.D. Song, "Design for Megavolt Inverse-Pinch Plasma Switch," (UNCLASSIFIED) *7th IEEE Pulsed Power Conference*, Monterey, CA, June 11-14, 1989, Paper P2-19, p. 717.(UNCLASSIFIED)
- 3 P.S. Anan'in, V.B. Karpov, Ya.E. Krasik, I.V. Lisitsyn, A.V. Petrov, and V.G. Tolmacheva, "Investigation of plasma opening switches with pulsed gas guns," (UNCLASSIFIED) *Sov. Phys. Tech. Phys.* **36**(8), 894 (1991).(UNCLASSIFIED)
- 4 General Valve Corporation, Fairfield New Jersey.(UNCLASSIFIED)
- 5 B.V. Weber, and D.D. Hinshelwood, "He-Ne interferometer for density measurements in plasma opening switch experiments," (UNCLASSIFIED) *Rev. Sci. Instrum.* **63**(10), 5199 (1992).(UNCLASSIFIED)
- 6 K. Bockasten, "Transformation of Observed Radiances into Radial Distribution of the Emission of a Plasma," (UNCLASSIFIED) *Opt. Soc. Amer.* **51**(9), 943 (1961).(UNCLASSIFIED)
- 7 B.V. Weber and S.F. Fulghum, "A high sensitivity two-color interferometer for pulsed power plasmas," (UNCLASSIFIED) *Rev. Sci. Instrum.* **68**(2), 1227 (1997).(UNCLASSIFIED)
- 8 R.J. Commisso, P.J. Goodrich, J.M. Grossmann, D.D. Hinshelwood, P.F. Ottinger, and B.V. Weber, "Characterization of a microsecond-conduction-time plasma opening switch," (UNCLASSIFIED) *Phys. Fluids B* **4**(7), 2369 (1992).(UNCLASSIFIED)
- 9 T.J. Renk, "Flashboards as a plasma source for plasma opening switch applications," (UNCLASSIFIED) *J. Appl. Phys.* **65**(7), 2652 (1989).(UNCLASSIFIED)

- 10 J.R. Goyer, D. Kortbawi, F.K. Childers, and P.S. Sincerny, "Low jitter operation of a plasma opening switch," (UNCLASSIFIED) J. Appl. Phys. **74**(6), 4236 (1993).
- 11 P.J. Goodrich, R.J. Comisso, J.M. Grossmann, D.D. Hinshelwood, R.A. Riley, S.B. Swanekamp, and B.V. Weber, "High Power Plasma Opening Switch Operation on Hawk," (UNCLASSIFIED) in *Proceeding of the 10th International Conference on High Power Particle Beams*, Vol. 1, p. 299.(UNCLASSIFIED)
- 12 B.V. Weber, D.D. Hinshelwood, and R.J. Comisso, "Interferometry of Flashboard and Cable-Gun Plasma Opening Switches on Hawk," (UNCLASSIFIED) IEEE Trans. Plasma Sci. **25**(2), 189 (1997).(UNCLASSIFIED)
- 13 W. Rix, D. Parks, J. Shannon, J. Thompson, and E. Waisman, "Operation and Empirical Modeling of the Plasma Opening Switch," (UNCLASSIFIED) IEEE Trans. Plasma Sci. **19**(2), 400 (1991).(UNCLASSIFIED)
- 14 B.V. Weber, R.J. Comisso, P.J. Goodrich, J.M. Grossmann, D.D. Hinshelwood, P.F. Ottinger, and S.B. Swanekamp, "Plasma opening switch conduction scaling," (UNCLASSIFIED) Phys. Plasmas **2**(10), 3893 (1995).(UNCLASSIFIED)
- 15 K.V. Chukbar and V.V. Yan'kov, "Evolution of the magnetic field in plasma opening switches," (UNCLASSIFIED) Sov. Phys. Tech. Phys. **33**(11), 1293 (1988). (UNCLASSIFIED)
- 16 J.R. Goyer, "A Conduction Model for PEOS Operation Incorporating Simplified Cathode Sheath Effects," (UNCLASSIFIED) IEEE Trans. Plasma Sci. **19**(5), 920 (1991).(UNCLASSIFIED)
- 17 Private communication, Dr. Yitzhak Maron, Plasma Analyses.(UNCLASSIFIED)

DISTRIBUTION LIST

DEPARTMENT OF DEFENSE

BALLISTIC MISSILE DEFENSE OFFICE
7100 DEFENSE PENTAGON
WASHINGTON, D.C. 20301-7100
ATTN: T/SL

DEFENSE ADVANCED RESEARCH
PROJECTS AGENCY
3701 NORTH FAIRFAX DRIVE
ARLINGTON, VA 22203-1714
ATTN: DED

COMMANDER
DEFENSE INFORMATION
SYSTEMS AGENCY
PACIFIC AREA
WHEELER AFB, HI 96854-5000
ATTN: COMMANDER

DEFENSE TECHNICAL
INFORMATION CENTER
8725 JOHN J. KINGMAN ROAD, SUITE 0944
FORT BELVOIR, VA 22060-6218
ATTN: DTIC/OCF

DEFENSE THREAT REDUCTION AGENCY
6801 TELEGRAPH ROAD
ALEXANDRIA, VA 22310-3398
ATTN: CPF, P. HEBERT
ATTN: CPWCT
ATTN: CPWP, T. KENNEDY
ATTN: CPWT
ATTN: NSC
ATTN: NSS, J. M. PIERRE
ATTN: NSSA, DR G. DAVIS
ATTN: NSSA, W. SUMMA
ATTN: NSSE, W. J. SCOTT
ATTN: NSSS, D. BELL
ATTN: NSSS, DR. K. WARE
ATTN: NSSS, L. PRESSLEY
ATTN: NSSS, R. GULLICKSON
ATTN: NSSS, R. MAINGER
ATTN: PMP
ATTN: SWWA

DEFENSE THREAT REDUCTION AGENCY
ALBUQUERQUE OPERATIONS
1680 TEXAS STREET, SE
KIRTLAND AFB, NM 87117-5669
ATTN: CPT-D DR. G. BALADI
ATTN: CPTO
ATTN: CPTO, R. W. SHOUP

PRESIDENT
NATIONAL DEFENSE UNIVERSITY
FORT LESLEY J. MCNAIR
WASHINGTON, DC 20319-6000
ATTN: NWCO

DIRECTOR
NET ASSESSMENT
OFFICE OF THE SEC OF DEFENSE
ROOM 3A930, THE PENTAGON
WASHINGTON, DC 20301
ATTN: DOCUMENT CONTROL

DEPARTMENT OF DEFENSE CONTRACTORS

AEROSPACE CORP
P. O. BOX 92957
LOS ANGELES, CA 90009
ATTN: LIBRARY ACQUISITION, M1/199
ATTN: M2/241, T. PARK

ALME AND ASSOCIATES
ATTN: DOC
P. O. BOX 4057
ALEXANDRIA, VA 22303
ATTN: J. F. DAVIS
ATTN: S. SEILER, G101

APTEK, INC.
1257 LAKE PLAZA DRIVE
COLORADO SPRINGS, CO 80906-3578
ATTN: T. MEAGHER

BERKELEY RSCH ASSOCIATES, INC.
P. O. BOX 852
SPRINGFIELD, VA 22150-0852
ATTN: N. PEREIRA

CHARLES STARK DRAPER LAB, INC.
555 TECHNOLOGY SQUARE
CAMBRIDGE, MA 02139
ATTN: LIBRARY, MS #74

DEFENSE GROUP, INC
P. O. BOX 7522
SANTA MONICA, CA 90406-7522
ATTN: R. POLL

E-SYSTEMS, INC.
ECI DIVISION
P. O. BOX 12248
ST. PETERSBURG, FL 33733-2248
ATTN: MS 3, TECH INFO CTR

HY-TECH RESEARCH CORPORATION
104 CENTRE COURT
RADFORD, VA 24141
ATTN: E. J. YADLOWSKY
ATTN: J. J. MOSCHELLA
ATTN: R. C. HAZELTON

ITT INDUSTRIES
ITT SYSTEMS CORPORATION
ATTN: AODTRA/DASIAC
1680 TEXAS STREET, SE
KIRTLAND AFB, NM 87117-5669
ATTN: DASIAC
ATTN: DASIAC/DARE

ITT SYSTEMS CORPORATION
2560 HUNTINGTON AVENUE
ALEXANDRIA, VA 22303
ATTN: C. FORE

JAYCOR
1410 SPRING HILL ROAD, SUITE 300
MCLEAN, VA 22102
ATTN: DR C. P. KNOWLES

JAYCOR
P. O. BOX 85154
SAN DIEGO, CA 92186-5154
ATTN: M. TREADAWAY

KTECH CORP.
2201 BUENA VISTA DRIVE, SE, SUITE 400
ALBUQUERQUE, NM 87106-4265
ATTN: F. DAVIES

LOGICON - RDA
2100 WASHINGTON BOULEVARD
ARLINGTON, VA 22204-5706
ATTN: E. QUINN
ATTN: I. VITKOVITSKY

MAXWELL PHYSICS INT'L COMPANY
2700 MERCED STREET
SAN LEANDRO CA 94577-0599
ATTN: B. FAILOR
ATTN: C. STALLINGS
ATTN: J. RIORDAN
ATTN: P. SINCERNY
ATTN: S. L. WONG

MAXWELL TECHNOLOGIES
8888 BALBOA AVENUE, BUILDING 1
SAN DIEGO, CA 92123
ATTN: J. THOMSON
ATTN: P. COLEMAN
ATTN: W. H. RIX

MISSION RESEARCH CORP.
1720 RANDOLPH ROAD, SE
ALBUQUERQUE, NM 87106-4245
ATTN: K. STRUVE

PULSE SCIENCES, INC.
600 MC CORMICK STREET
SAN LEANDRO, CA 94577
ATTN: I. D. SMITH
ATTN: P. W. SPENCE
ATTN: TECHNICAL LIBRARY

SCIENCE APPLICATIONS INTL. CORP.
P. O. BOX 1303
MCLEAN, VA 22102
ATTN: W. CHADSEY

SRI INTERNATIONAL
333 RAVENSWOOD AVENUE
MENLO PARK, CA 94025-3434
ATTN: ELECTROMAG SCI LAB TECH LIB

SVERDRUP INC., AEDC
253 1ST STREET
ARNOLD AFB, TN 37389-2250
ATTN: L. S. CHRISTENSEN, MS 640

SVERDRUP TECHNOLOGY INC.
P. O. BOX 884
TULLAHOMA, TN 37388
ATTN: V. KENYON

TEXAS TECH UNIVERSITY
PULSED POWER LAB
PHYSICS DEPARTMENT
LUBBOCK, TX 79409
ATTN: L. HATFIELD, M/S 1051
ATTN: M. KRISTIANSEN, M/S 3102

DEPARTMENT OF ENERGY

UNIVERSITY OF CALIFORNIA
LAWRENCE LIVERMORE NATIONAL LAB
P. O. BOX 808
LIVERMORE, CA 94551-9900
ATTN: L-031, L. SUTER
ATTN: L-180, G. SIMONSON

LOS ALAMOS NATIONAL LABORATORY
P. O. BOX 1663
LOS ALAMOS, NM 87545
ATTN: F-670, C. EKDAHL
ATTN: MS D408
ATTN: MS H827
ATTN: MS-J970/R. REINOVSKY

HY-TECH RESEARCH CORPORATION
104 CENTRE COURT
RADFORD, VA 24141
ATTN: E. J. YADLOWSKY
ATTN: J. J. MOSCHELLA
ATTN: R. C. HAZELTON

ITT INDUSTRIES
ITT SYSTEMS CORPORATION
ATTN: AODTRA/DASIAC
1680 TEXAS STREET, SE
KIRTLAND AFB, NM 87117-5669
ATTN: DASIAC
ATTN: DASIAC/DARE

ITT SYSTEMS CORPORATION
2560 HUNTINGTON AVENUE
ALEXANDRIA, VA 22303
ATTN: C. FORE

JAYCOR
1410 SPRING HILL ROAD, SUITE 300
MCLEAN, VA 22102
ATTN: DR C. P. KNOWLES

JAYCOR
P. O. BOX 85154
SAN DIEGO, CA 92186-5154
ATTN: M. TREADAWAY

KTECH CORP.
2201 BUENA VISTA DRIVE, SE, SUITE 400
ALBUQUERQUE, NM 87106-4265
ATTN: F. DAVIES

LOGICON - RDA
2100 WASHINGTON BOULEVARD
ARLINGTON, VA 22204-5706
ATTN: E. QUINN
ATTN: I. VITKOVITSKY

MAXWELL PHYSICS INT'L COMPANY
2700 MERCED STREET
SAN LEANDRO CA 94577-0599
ATTN: B. FAILOR
ATTN: C. STALLINGS
ATTN: J. RIORDAN
ATTN: P. SINCERNY
ATTN: S. L. WONG

MAXWELL TECHNOLOGIES
8888 BALBOA AVENUE, BUILDING 1
SAN DIEGO, CA 92123
ATTN: J. THOMSON
ATTN: P. COLEMAN
ATTN: W. H. RIX

MISSION RESEARCH CORP.
1720 RANDOLPH ROAD, SE
ALBUQUERQUE, NM 87106-4245
ATTN: K. STRUVE

PULSE SCIENCES, INC.
600 MC CORMICK STREET
SAN LEANDRO, CA 94577
ATTN: I. D. SMITH
ATTN: P. W. SPENCE
ATTN: TECHNICAL LIBRARY

SCIENCE APPLICATIONS INTL. CORP.
P. O. BOX 1303
MCLEAN, VA 22102
ATTN: W. CHADSEY

SRI INTERNATIONAL
333 RAVENSWOOD AVENUE
MENLO PARK, CA 94025-3434
ATTN: ELECTROMAG SCI LAB TECH LIB

SVERDRUP INC., AEDC
253 1ST STREET
ARNOLD AFB, TN 37389-2250
ATTN: L. S. CHRISTENSEN, MS 640

SVERDRUP TECHNOLOGY INC.
P. O. BOX 884
TULLAHOMA, TN 37388
ATTN: V. KENYON

TEXAS TECH UNIVERSITY
PULSED POWER LAB
PHYSICS DEPARTMENT
LUBBOCK, TX 79409
ATTN: L. HATFIELD, M/S 1051
ATTN: M. KRISTIANSEN, M/S 3102

DEPARTMENT OF ENERGY

UNIVERSITY OF CALIFORNIA
LAWRENCE LIVERMORE NATIONAL LAB
P. O. BOX 808
LIVERMORE, CA 94551-9900
ATTN: L-031, L. SUTER
ATTN: L-180, G. SIMONSON

LOS ALAMOS NATIONAL LABORATORY
P. O. BOX 1663
LOS ALAMOS, NM 87545
ATTN: F-670, C. EKDAHL
ATTN: MS D408
ATTN: MS H827
ATTN: MS-J970/R. REINOVSKY

SANDIA NATIONAL LABORATORIES

ATTN: MAIL SERVICES

P. O. BOX 5800

ALBUQUERQUE, NM 87185-0459

ATTN: C. DEENEY, MS 1194

ATTN: D. COOK, MS 1190

ATTN: D. MACDANIEL, MS 1194

ATTN: M. HEDEMAN, MS 1159

ATTN: M. K. MATZEN, MS 1187

ATTN: TECHNICAL LIBRARY, MS 0899

ATTN: W BALLARD, MS 1179

ATTN: W BEEZHOLD, MS-1155

U S DEPT OF ENERGY IE-24

1000 INDEPENDENCE AVENUE, SW

WASHINGTON, DC 20585

ATTN: D. CRANDALL

U.S. DEPARTMENT OF ENERGY

P. O. BOX A

GERMANTOWN, MD 20875-0963

ATTN: C. B. HILLAND, DP-243

ATTN: C. KEANE, DP-16

ATTN: OMA/DP-252, R. GUNDERSON

DEPARTMENT OF THE AIR FORCE

AFIWC/MSO

102 HALL BOULEVARD SUITE 315

SAN ANTONIO, TX 78243-7016

ATTN: TECHNICAL LIBRARY

AIR FORCE FOR STUDIES & ANALYSIS

1570 AIR FORCE PENTAGON

WASHINGTON, DC 20330-1570

ATTN: SATI, RM 1D363

AIR FORCE RESEARCH LABORATORY

3550 ABERDEEN AVENUE, SE

KIRTLAND AFB, NM 87117-5776

ATTN: PLWSP, J KIUTTU

ATTN: WSP/J DEGNAN

AIR UNIVERSITY LIBRARY

600 CHENNAULT CIRCLE

BUILDING 1405, ROOM 160

MAXWELL AFB, AL 36112-6424

ATTN: AUL-LSE

ARNOLD ENGINEERING

DEVELOPMENT CENTER

1099 AVENUE C

ARNOLD AFB, TN 37389-9011

ATTN: K. BRANDON

SAN ANTONIO AIR LOGISTICS CTR

DIRECTORATE OF SPECIAL WEAPONS

KELLY AFB, TX 78241-5000

ATTN: ALC/SW, F. CRISTADORO

USAF ROME LABORATORY

TECHNICAL LIBRARY, FL2810

CORRIDOR W. SUITE 262, RL/SUL

26 ELECTRONICS PARKWAY, BUILDING 106

GRIFFIS AFB, NY 13441-4514

ATTN: RBCM

ATTN: RBCT

DEPARTMENT OF THE ARMY

DEPARTMENT OF THE ARMY

DEPUTY CHIEF OF STAFF FOR

OPERATIONS AND PLANS

PENTAGON

WASHINGTON, DC 20310-0460

ATTN: DAMO-ODW

US ARMY RESEARCH LABORATORIES

2800 POWDER MILL ROAD

ADELPHI, MD 20783-1197

ATTN: TECHNICAL LIBRARY

ATTN: AMSEL-WT-NH/KEHS

ATTN: AMSRL-WT-KEHS

COMMANDER

US ARMY SPACE & STRATEGIC DEFENSE

COMMAND

CSSD-TC-SR

P. O. BOX 1500

HUNTSVILLE, AL 35807-3801

ATTN: CSSD-ES-E1, R. CROWSON

US ARMY THAAD PROJECT OFFICE

P. O. BOX 1500

HUNTSVILLE, AL 35807-3801

ATTN: CSSD-WD

COMMANDER

US ARMY VULNERABILITY

ASSESSMENT LABORATORY

WHITE SANDS MISSILE RANGE, NM

88002-5513

ATTN: SLCVA-TAC

DEPARTMENT OF THE NAVY

COMMANDER
NAVAL AIR SYSTEMS COMMAND
47123 BUSE ROAD, #IPT
PATUXENT RIVER, MD 20670
ATTN: AIR 5161
ATTN: AIR-5164
ATTN: AIR-933

NAVAL RESEARCH LABORATORY
4555 OVERLOOK AVENUE, SW
WASHINGTON, DC 20375-5000
ATTN: CODE 6720, J. DAVIS
ATTN: CODE 6770, G. COOPERSTEIN

COMMANDER
NAVAL SURFACE WARFARE CENTER
DAHLGREN DIVISION
17320 DAHLGREN ROAD
DAHLGREN, VA 22448-5000
ATTN: B. DEPARTMENT

OFFICE OF NAVAL INTELLIGENCE
4251 SUITLAND ROAD
WASHINGTON, DC 20395-5720
ATTN: DEOO
ATTN: LIBRARY

COMMANDER
SPACE & NAVAL WARFARE SYSTEMS CMD
DEPARTMENT OF THE NAVY
2451 JEFFERSON DAVIS HIGHWAY
ARLINGTON, VA 22245
ATTN: PMW-145

DIRECTOR
STRATEGIC SYSTEMS PROGRAMS
37224 TRIDENT
1931 JEFFERSON DAVIS HIGHWAY
ARLINGTON, VA 22202-5362
ATTN: J. BURTLE
ATTN: K. TOBIN

OTHER GOVERNMENT

CENTRAL INTELLIGENCE AGENCY
WASHINGTON, DC 20505
ATTN: OSWR, J. PINA
ATTN: OSWR/SSD/SWB
ATTN: OSWR/STD/TTB

FEDERAL EMERGENCY MANAGEMENT AGENCY
500 C. STREET, SW, SUITE 514
WASHINGTON, D.C. 20472
ATTN: SL-CD-MP

DIRECTOR
NATIONAL SECURITY AGENCY
FORT GEORGE G. MEADE, MD 20755-6000
ATTN: TECHNICAL LIBRARY